



**HAL**  
open science

# Influence of time, temperature, confining pressure and fluid content on the experimental compaction of spherical grains

Magali Rossi, Olivier Vidal, Bernd Wunder, François Renard

► **To cite this version:**

Magali Rossi, Olivier Vidal, Bernd Wunder, François Renard. Influence of time, temperature, confining pressure and fluid content on the experimental compaction of spherical grains. *Tectonophysics*, 2007, 441, pp.47-65. 10.1016/j.tecto.2007.05.001 . hal-00201796

**HAL Id: hal-00201796**

**<https://hal.science/hal-00201796>**

Submitted on 3 Jan 2008

**HAL** is a multi-disciplinary open access archive for the deposit and dissemination of scientific research documents, whether they are published or not. The documents may come from teaching and research institutions in France or abroad, or from public or private research centers.

L'archive ouverte pluridisciplinaire **HAL**, est destinée au dépôt et à la diffusion de documents scientifiques de niveau recherche, publiés ou non, émanant des établissements d'enseignement et de recherche français ou étrangers, des laboratoires publics ou privés.

1 **Influence of time, temperature, confining pressure and fluid content on the experimental**  
2 **compaction of spherical grains**

3

4 M. Rossi<sup>\*1,a</sup>, O. Vidal<sup>1</sup>, B. Wunder<sup>2</sup>, F. Renard<sup>3</sup>

5

6 <sup>1</sup> Laboratoire de Géodynamique des Chaînes Alpines, CNRS, OSUG, Université Joseph  
7 Fourier, BP 53, 38 041 Grenoble Cedex 9, France

8 Fax: +33 4 76 51 40 58, E-mail addresses: mrossi@ujf-grenoble.fr, ovidal@ujf-grenoble.fr

9

10 <sup>2</sup> GeoForschungsZentrum Potsdam, Division 4.1, Telegrafenberg, 14473 Potsdam, Germany

11 Fax: +49 331 288 1402, E-mail adress: wunder@gfz-potsdam.de

12

13 <sup>3</sup> Laboratoire de Géophysique Interne et de Tectonophysique, CNRS, OSUG, Université  
14 Joseph Fourier, BP 53, 38 041 Grenoble Cedex 9, France

15 Fax: +33 4 76 82 81 01, E-mail address: frenard@obs.ujf-grenoble.fr

16

17 \* Corresponding author

18 Phone: +33 (0)4 79 75 94 28

19 Fax: +33 (0)4 79 75 87 77

20 E-mail address: Magali.Rossi@univ-savoie.fr

21 <sup>a</sup> Present address: Environnement Dynamique et Territoires de Montagnes, UMR CNRS  
22 5204, Bât. Belledonne, Université de Savoie, F-73373 Le Bourget du Lac, France.

23

24

25 **Abstract**

26 Theoretical models of compaction processes, such as for example intergranular  
27 pressure-solution (IPS), focus on deformation occurring at the contacts between spherical  
28 grains that constitute an aggregate. In order to investigate the applicability of such models,  
29 and to quantify the deformation of particles within an aggregate, isostatic experiments were  
30 performed in cold-sealed vessels on glass sphere aggregates at 200 MPa confining pressure  
31 and 350°C with varying amounts of fluid. Several runs were performed in order to investigate  
32 the effects of time, fluid content, pressure and temperature, by varying one of these  
33 parameters and holding the others fixed. In order to compare the aggregates with natural  
34 materials, similar experiments were also performed using quartz sand instead of glass spheres.  
35 Experiments with quartz show evidence of IPS, but the strain could not be quantified.  
36 Experiments with glass spheres show evidence of several types of deformation process: both  
37 brittle (fracturing) and ductile (plastic flow and fluid-enhanced deformation, such as IPS). In  
38 experiments with a large amount of water ( $\geq 5$  vol.%), dissolution and recrystallization of the  
39 glass spheres also occurred, coupled with crystallization of new material filling the initial  
40 porosity. Experiments performed with a fluid content of less than 1 vol.% indicate creep  
41 behavior that is typical of glass deformation, following an exponential law. These  
42 experiments can also be made to fit a power law for creep, with a stress exponent of  
43  $n = 10.5 \pm 2.2$  in both dry and wet experiments. However, the pre-factor of the power law  
44 creep increases 5 times with the addition of water, showing the strong effect of water on the  
45 deformation rate. These simple and low-cost experiments provide new insights on the  
46 rheology of plastically deformed aggregates, which are found in many geological  
47 environments, such as partially molten-rocks, pyroclastic deposits or fault gouges during the  
48 inter-seismic period.

49

50 **Keywords:** isostatic experiments, glass spheres, ductile deformation, compaction

51

52 **1 Introduction**

53 Ductile deformation usually occurs in the lower crust under high pressure (P) and  
54 temperature (T) conditions by crystal plasticity, but can also be efficient under mid-crustal P-  
55 T conditions when deformation is accommodated by diffusive mass transfer through a fluid  
56 phase (intergranular pressure-solution – IPS – ; e.g., Weyl 1959; Rutter, 1976; Tada & Siever  
57 1989; Gratier *et al.* 1999). IPS results from a stress gradient at grain-scale that leads to

58 dissolution and flattening of grain contacts, transport through the contacts to the pores, and  
59 precipitation of new phases within the porosity (e.g., Weyl 1959; Tada & Siever 1989). At  
60 higher confining pressure, plastic deformation can occur at grain contacts leading to contact  
61 flattening. These two ductile deformation mechanisms thus compact and strengthen the initial  
62 aggregate, leading to a reduction in porosity and permeability.

63 Numerous experimental studies have been performed in order to understand the  
64 mechanical processes and to quantify the strain of mineral aggregates. High-temperature  
65 compaction experiments have been performed in order to investigate plastic deformation in  
66 the lower crust and in high-strain zones using both dry and hydrated aggregates (e.g., Rybacki  
67 & Dresen, 2000; Xiao *et al.*, 2002; Rutter & Brodie, 2004). Under the P-T conditions of the  
68 middle and upper crust, creep experiments were performed in the presence of fluid, including  
69 1) compaction experiments in drained conditions, (e.g., Renton *et al.* 1969; Rutter 1983;  
70 Kronenberg & Tullis 1984; Gratier & Guiguet 1986; Rutter & Wanten 2000), 2) compaction  
71 experiments with a controlled fluid pressure (i.e. the effective pressure: Niemeijer *et al.* 2002;  
72 Niemeijer & Spiers 2002; He *et al.*, 2003), and 3) shearing experiments (Bos & Spiers, 2000;  
73 Stünitz & Tullis 2001).

74 Supplementing the experimental approaches, several numerical and theoretical models  
75 have been proposed to explain creep compaction (e.g. Weyl, 1959; Rutter, 1976; Raj &  
76 Chyung 1981; Tada & Siever 1986; Tada *et al.* 1987). These models are generally based on  
77 the deformation of spherical elements making up an aggregate (e.g., Lemée & Guéguen,  
78 1996; Renard *et al.* 1999, 2000; Gundersen *et al.* 2002; Yasuhara *et al.* 2003). The  
79 comparison between models, experiments and nature is not straightforward because  
80 compaction experiments are generally conducted with grains of irregular shape, and because  
81 models focus on the grain-scale deformation, whereas compaction experiments focus on bulk  
82 deformation of the aggregate.

83 Considering an aggregate in a closed system, subjected to an external hydrostatic  
84 pressure, the effective normal stress at the grain contacts depends on the external confining  
85 pressure, the pore fluid pressure, and the contacts surface area that increases with compaction.  
86 Therefore, the final morphology of the spheres and the size of the contact areas can be used to  
87 estimate the local effective stress at the grain contacts at the end of experimental runs.  
88 Experiments of different run times involving calibrated spheres instead of grains of irregular  
89 shape, conducted in closed systems with different starting solid/fluid ratios could be used to  
90 quantify strain at the particle scale and to constrain general strain-stress relations, even  
91 without a proper knowledge of the applied stress or strain rate. The aim of the present study

92 was to test this “grain-scale” approach by conducting compaction experiments on an  
93 aggregate of calibrated spherical particles, in order to quantify particle strain at the end of the  
94 runs by observing the grain contacts using a Scanning Electron Microscope (SEM).

95         Such experiments could be conducted using very simple experimental equipment, such  
96 as isostatic cold-sealed autoclaves or internally-heated apparatus, thus reducing the duration  
97 of experiment preparation, and allowing experiments to be performed over a wide range of  
98 confining pressure and temperature values. The main disadvantage of such an experimental  
99 set-up is the change in effective stress during the experiment, due to an increase in the contact  
100 surface area between the spheres with increasing compaction. Therefore, the strain rate and  
101 the stress at the contacts are not controlled and vary during the experiment, making it difficult  
102 to derive general compaction laws. However, the combination of experiments conducted with  
103 the same initial conditions (sphere diameter, water/sphere ratio, temperature, and confining  
104 pressure) but different run durations should allow the time-dependent change in strain rate  
105 and local stress to be estimated at the contact of the spheres with deformation. To the authors'  
106 knowledge, such an approach has not been attempted so far as it requires working with  
107 aggregates with constant particle geometry and size. Owing to the difficulties in producing  
108 perfectly spherical mineral grains with a small and constant size of about 100  $\mu\text{m}$ , which are  
109 required for such experiments, commercial glass spheres had to be used. Moreover,  
110 dissolution and precipitation kinetics of glass are higher than in crystallized materials, thus  
111 allowing shorter experimental durations.

112         The present work reports on experiments conducted in closed system conditions  
113 varying the time, the solid/fluid ratio, the confining pressure and the temperature. The results  
114 open up the possibility of studying rock deformation under isostatic confining pressure, and  
115 using glass spheres as an analogous material for silicate minerals. For comparison with  
116 natural minerals, similar experiments were conducted with non-spherical quartz grains instead  
117 of glass spheres. The results obtained from this very simple experimental approach are used to  
118 discuss the creep law of an aggregate made of ductile glass beads and the controlling effect of  
119 water content, temperature and pressure on deformation.

120

## 121 **2 Experimental method**

122         The starting material was an aggregate of 45-90  $\mu\text{m}$  diameter spheres of soda-lime  
123 glass (72%  $\text{SiO}_2$ , 14%  $\text{Na}_2\text{O}$ , 10%  $\text{CaO}$  and 3%  $\text{MgO}$ ) from Sandmaster-France. At  
124 atmospheric pressure this glass has a softening point at 730°C. According to figure 1, and  
125 assuming that viscosity increases with pressure, the glass should behave elastically under

126 stress at  $T < 450^{\circ}\text{C}$ . Therefore, and since it is the IPS processes that were of prime interest,  
127 most experiments were conducted at  $350^{\circ}\text{C}$  and 200 MPa confining pressure. For comparison  
128 with crystallized material, additional experiments were performed with quartz sand (Nemours  
129 sand;  $d_{50}=199\ \mu\text{m}$ ). In order to investigate the variation in strain with time, several runs were  
130 made at the same P-T conditions for durations ranging from 2 hours to 4 weeks. To  
131 investigate the effect of temperature at constant pressure, a set of experiments was conducted  
132 at 25, 150, 250, 350 and  $450^{\circ}\text{C}$  and a constant pressure of 200 MPa. The effect of pressure  
133 was studied at a constant temperature of  $350^{\circ}\text{C}$ , with experiments conducted at 100, 200, 300  
134 and 400 MPa (table 1).

135 In all experiments, the glass spheres (or quartz grains) were mixed with about 3 wt.%  
136 biotite to investigate the possible enhancement of IPS at the contacts with phyllosilicates (Bos  
137 & Spiers, 2000; Rutter & Wanten, 2000; Niemeijer & Spiers, 2002). 100 mg of this was  
138 loaded with varying but controlled amounts of fluid into a 3.0 mm outside diameter, 0.2 mm  
139 wall thickness and 12 mm long cylindrical gold capsule (figure 2A). The confining pressure  
140 minus the pressure of the water in the capsule equals the effective confining pressure. To  
141 investigate the effect of fluid availability on deformation, various amounts of fluid were thus  
142 introduced in the sample: 0, 1 and 5 vol.% double de-ionized water (volume of fluid related to  
143 100% volume of glass spheres). These amounts of water give rise to different fluid ( $P_f$ ) and  
144 effective ( $P_e$ ) pressures. Assuming a body-centered cubic packing, the starting porosity of the  
145 sphere aggregate is about 32%. Considering an initial porosity of 32%, the density of the air +  
146 water fluid in the 5 vol.% water experiments was  $0.12\ \text{g}\cdot\text{cm}^{-3}$ . From the P-V-T data of  
147 Burnham *et al.* (1969) and Keenan *et al.* (1969), this corresponds to a  $P_f \sim 25\ \text{MPa}$  at  $450^{\circ}\text{C}$ .  
148 The  $0.12\ \text{g}\cdot\text{cm}^{-3}$  iso-density curve intersects the vapor-liquid equilibrium curve at about  $350^{\circ}\text{C}$   
149 and 17 MPa. Below this temperature,  $P_f$  lies on the liquid-vapor curve, i.e. about 10 MPa at  
150  $300^{\circ}\text{C}$  and 4 MPa at  $150^{\circ}\text{C}$ . Experiments performed with 20 vol.% of fluid at  $400^{\circ}\text{C}$  would  
151 thus have a fluid pressure of about 40 MPa. Therefore, the fluid pressure in the 1 to 5 water  
152 vol.% experiments was about 12% of the confining pressure ( $P_c$ ), and  $P_f < 0.1 \times P_c$  in  
153 experiments conducted at  $T < 400^{\circ}\text{C}$ . The fluid pressure was higher in experiments conducted  
154 with higher amounts of fluid, but it was always less than  $0.25 \times P_c$  (maximum value  
155 calculated for the  $400^{\circ}\text{C}$  experiment performed with 20 vol.% fluid). These calculations show  
156 that the effective pressure was almost the same or close to the confining pressure in most  
157 experiments.

158 Gold capsules were used because gold is not reactive to the materials and fluids used  
159 for this study. Moreover, gold deforms easily and the external confining pressure is

160 completely transmitted to the enclosed experimental mixture. Once filled, the capsules were  
161 welded shut and placed in a water-pressurized horizontal cold-sealed pressure vessel (Tuttle,  
162 1969; figure 2B). The capsules were weighed after each stage of sample preparation to check  
163 for any leakage. Confining pressure was measured to within  $\pm 5$  MPa, and temperature was  
164 measured to within  $\pm 1^\circ\text{C}$  with a chromel-alumel thermocouple located inside the vessel at the  
165 contact with the gold capsule. Because of the strong inertia of the heating system and the  
166 small size of the capsule, the temperature gradient at the hot end of the autoclave and along  
167 the capsule was negligible (Vidal, 1997; Vidal & Durin, 1999).

168 In each experiment, pressure was applied first, and the sample was then heated up to  
169 the desired temperature in about two hours, keeping the pressure constant. At the end of the  
170 runs, temperature was decreased to  $25^\circ\text{C}$  in less than 15 minutes. The remaining pressure was  
171 released when the samples had reached room temperature.

172 After the runs, the capsules were weighed to check for any water loss and leakage. The  
173 capsules were then opened and some material was collected for SEM observation. Except for  
174 experiments performed with  $\geq 5$  vol.% fluid, aggregate cohesion was lost during this  
175 procedure, which facilitated observations of the grain contact size and morphology. The run  
176 material was deposited on gold-coated copper holders and observed with a Zeiss DSM 962  
177 SEM (GFZ Potsdam, Germany) and a Leica Stereoscan 440 SEM (Université de Savoie,  
178 Chambéry, France). Local strain at the grain contacts was calculated from the change in grain  
179 geometry measured on the SEM pictures (see part 3.2). The amount of fluid that possibly  
180 entered the glass spheres during the experiments was estimated qualitatively from Raman  
181 spectroscopy, using a Jobin-Yvon LabRam HR800 (ENS-Lyon, France), conducted directly  
182 on the spheres or on double polished thin sections made from epoxy-impregnated samples.

183

### 184 **3 Results**

#### 185 *3.1 Effect of water content on the morphology of contacts*

186 The morphology of the grain-grain contacts characterized under the SEM is strongly  
187 dependent on the amount of fluid within the sample.

188 *In dry experiments*, the contacts between the grains showed flat circular morphologies  
189 (figure 3A) and the spheres were not bound together. Despite flattening at the contact, there  
190 was no significant reduction in porosity after the runs. *In experiments with 1 vol.% fluid*, most  
191 spheres were bound together and the contacts showed a flat rim and conchoidal cracking at  
192 the core (figure 3B). Numerous contacts showed concentric circles of alternating outgrowths  
193 and depressions (figure 3C), and rare stylolite-like contacts were observed, with the spheres

194 both dissolving and penetrating one into another (figure 3D). In both dry and 1 vol.% fluid  
195 experiments, the initial porosity was well maintained despite deformation: porosity reduction  
196 was too small to be observed under the SEM (figure 3A-B). On the contrary, the initial  
197 porosity *in experiments conducted with  $\geq 5$  vol.% fluid* was completely filled with a  
198 microporous matrix having the same composition as the glass spheres. The spheres were all  
199 bound together, and their free faces showed recrystallized rims (figure 3E-F). Porosity filling  
200 and sphere bonding combined to strengthen the material. The sphere diameter was slightly  
201 smaller than that of the starting material, and sphere interpenetration was observed, both these  
202 phenomena suggesting strong dissolution of the glass during the experiments. A further  
203 increase in the amount of fluid produced the same contact morphology, but also increased the  
204 reactivity of glass. Complete recrystallization of the spheres was observed in experiment  
205 ENS2 conducted with 15 vol.% fluid (figure 3G).

206 Raman spectroscopy was used to check the possible incorporation of water in the glass  
207 spheres and newly formed material in the porosity. Raman spectra of the initial glass spheres  
208 indicated that they were water-free (figure 4Aa). *In experiments with 1 vol.% fluid*, very  
209 smooth peaks were detected in the spectral range of water ( $3500 - 3750 \text{ cm}^{-1}$ ), indicating that  
210 if any, only a very small amount of water was absorbed at the rim of the spheres (figure 4Aa).  
211 The Raman spectra of the material filling the porosity *in experiments with 5 vol.% fluid*  
212 showed well-defined bands at  $3550\text{-}3750 \text{ cm}^{-1}$ ,  $615$  and  $1100 \text{ cm}^{-1}$  (figure 4A), which are  
213 characteristic of a hydrous crystalline phase. From comparison of the Raman spectra, this  
214 material resembles a Ca-bearing zeolite (figure 5), even though it is Al-free. A profile from  
215 this recrystallized material towards and through a glass sphere shows that glass hydration and  
216 recrystallization also occur at the rim of the glass spheres (figure 4B). At the contact between  
217 two glass spheres, neither glass crystallization nor glass hydration was observed or detected  
218 (figure 4B). These observations suggest that glass hydrolysis was associated with  
219 recrystallization. Furthermore, the initial macroporosity disappeared and was replaced by a  
220 fluid-rich microporous recrystallized matrix. At the sphere contacts, the availability of water  
221 was much lower than on the free surfaces. Therefore, no water was incorporated in the glass  
222 and no recrystallization occurred.

223 Regardless of the amount of fluid, evidence of cracking was found in some spheres in  
224 all experiments with the cracks spreading from one sphere contact to the next (figure 3H).  
225 Cracking increased significantly at low temperature and high confining pressure, but no  
226 relationship could be found between the amount of fluid and the amount of cracking. The  
227 timing of crack formation remains uncertain. Most cracks probably formed during the very



228 first stage of the experiments during pressure loading, and at the end of the experiments  
229 during quenching. However, cracks might also have been formed during the runs.

230 The occurrence of all the features previously described indicates at least three main  
231 responses to stress: ductile deformation in experiments performed with no or a small amount  
232 of fluid ( $\leq 1$  vol.%), brittle deformation in all runs, and chemical reaction (dissolution-  
233 crystallization) in experiments with a large amount of fluid ( $\geq 5$  vol.%).

234

### 235 3.2 *Time-dependent change in strain and T, P, water content dependency*

236 1-D strain was estimated from the change in diameter of the glass beads under  
237 compaction (figure 6A). Since the changes in the average sphere diameter due to compaction  
238 were negligible, the 1-D strain associated with each contact ( $\epsilon$ , shortening of the sphere radius  
239 at the contact) can therefore be calculated using the following relation:

$$240 \quad |\epsilon| = \frac{d_s - \sqrt{d_s^2 - d_c^2}}{d_s} \quad (1)$$

241 where  $d_c$  is the contact diameter and  $d_s$  the associated sphere diameter directly measured for  
242 each sphere on the SEM pictures (figure 6A). The size of the glass spheres  $d_s$  and the contact  
243 size  $d_c$  were determined from SEM pictures of the run products. Only unfractured and  
244 unbroken contacts were measured in order to estimate ductile strain. For each experiment,  
245 about 100 contacts were measured to calculate average contact diameters ( $N_c$  in table 1), to  
246 ensure that the local strain measured at different grain contacts is representative of the overall  
247 strain of the aggregate. Since the confining pressure was isotropic, the strain was also  
248 assumed to be isotropic. Equation 1 was only used to estimate the strain in dry experiments  
249 and experiments with 1 vol.% fluid for  $T \leq 350$  °C, i.e., experiments for which no glass  
250 recrystallization occurred. In experiments with 5 vol.% fluid or with 1 vol.% fluid at 450°C,  
251 the material is not loose and just a few sections of contacts could be observed with SEM. It  
252 was thus not possible to obtain a good statistical representation of the strain, which would  
253 thus be extremely badly constrained.

254 From equation 1 the finite strain at each contact was calculated at the end of the runs  
255 and the strain averaged over a significant number of contacts to obtain the overall strain  
256 achieved in each experiment (table 1). Figure 6B shows that in all experiments, most  
257 deformation occurred at the very beginning of the experiments, during the first ten hours.  
258 Then, deformation quickly slowed down after a few hours. Deformation-time relations were  
259 derived by combining the results obtained from different run-time experiments conducted

260 under the same P-T conditions and fluid/solid ratio (table 1, figure 6B). During the first two  
261 hours of each experiment, a strong increase in sphere contact area was observed, which  
262 implies a strong decrease in stress and strain rate. For this reason, the  $\varepsilon = f(t)_{[P,T]}$  relations  
263 were fitted with time-dependent power laws using only the strain data at  $t > 2$  hours. A power  
264 law exponent value of 0.068 is best constrained by the 1vol.% water experiments at 350°C  
265 (figure 6B). In view of the wide scatter of the values obtained in all the experiments, this  
266 power exponent was left unchanged to fit the other experiments. For the 150°C experiments,  
267 both the wet and dry experiments were fitted using the same  $\varepsilon = \alpha t^{0.068}$  function (dashed line  
268 in figure 6B). Then, discrete differentiation of the  $\varepsilon$ -time relation data at given P and T values  
269 gives the microscopic strain rate (values listed in table 1).

270 At 350°C, strain was clearly greater in the 1 vol.% fluid experiments than in the dry  
271 experiments, whereas the addition of water in the 150°C experiments did not show any  
272 significant difference compared to the dry experiments. The strain versus time plots in figure  
273 6B show that strain increased significantly with temperature. This can also be seen in figure 7,  
274 which shows a plot of the strain observed after 6 hours in experiments conducted at a pressure  
275 of 200 MPa, and temperatures of 25, 150, 250, 350 and 450°C. At  $T \geq 250^\circ\text{C}$  strain is  
276 enhanced by the addition of water. No quantitative data are available for the 1 vol.% fluid  
277 experiment performed at 450°C. Indeed, as observed at 350°C in experiments with 5 vol.%,  
278 the spheres chemically reacted with the fluid and the porosity was filled with new material.

279 A set of experiments with 6-hour run time was also performed at various confining  
280 pressures (100, 200, 300, 400 MPa) at 350°C (figure 8). As expected from the previous  $\varepsilon$ -T  
281 results after 6 hours, experiments containing 1 vol.% fluid showed a higher strain than dry  
282 experiments at all pressures. Radial fracturing spreading from the contacts increases with  
283 confining pressure (figure 3H), so that the number of contacts between unbroken spheres is  
284 lower in experiments with high rather than low confining pressure. However, figure 8 shows  
285 that, for a constant water content, the average strain increases linearly with increasing  
286 confining pressure.

287 All these observations indicate that strain increases with temperature, confining  
288 pressure, and the addition of even very small amounts of water. The similarity observed at  
289 350°C in 5 vol.% fluid experiments and at 450°C in 1 vol.% fluid experiments, and the fact  
290 that, at 150°C, dry and 1 vol.% fluid experiments have similar strain-time variations, suggest  
291 that the effect of water was thermally activated. In contrast, the effect of pressure was similar

292 for the dry and 1 vol.% fluid experiments. The observed increase in strain was thus simply  
293 related to an increase in local stress at the contact between the spheres.

294

### 295 3.3 *Effect of phyllosilicates*

296 3 wt.% biotite was introduced in the starting mixture, in order to investigate whether  
297 or not the presence of mica enhances deformation as discussed in the literature (Rutter 1983;  
298 Tada & Siever, 1989; Dewers & Ortoleva 1995; Hickman & Evans 1995; Bos *et al.* 2000;  
299 Rutter & Wanten 2000; Renard *et al.* 2001; Niemeijer & Spiers 2002). Glass sphere – mica  
300 contacts were scarce and difficult to identify because the samples lost their cohesion when  
301 opening the capsule. In dry experiments, the mica deformed mechanically by kinking and  
302 indentation (figure 9A). In experiments with 1 vol.% fluid, the mica was also kinked (figure  
303 9B) and the spheres were slightly dissolved at their contacts (figure 9C). The mica could also  
304 be dissolved when a fine flake was sandwiched between two spheres. In experiments with  
305 5 vol.% fluid, it was not possible to make any systematic direct observations of the mica  
306 because the mica flakes were closely sandwiched inside an aggregate of very compact  
307 recrystallized glass spheres. Some spheres were occasionally truncated at their contacts with  
308 mica (figure 9D), but it was hardly possible to quantify any strain or dissolution of these  
309 spheres. If at all, the dissolution of glass spheres at the contact with mica was low, and mica  
310 also dissolved.

311 Even though glass sphere dissolution was evidenced at the contact with the mica, it  
312 was impossible to quantify the amount of dissolution and the resulting strain related to the  
313 presence of mica. However SEM observations seemed to indicate that the effect of mica on  
314 glass sphere dissolution was mostly limited to spheres directly in contact with the mica flakes.

315

### 316 3.4 *Comparison with natural materials*

317 In order to compare the results obtained for glass spheres with natural materials,  
318 several experiments were carried out using natural quartz under the same P-T and water  
319 content conditions as used with the glass beads (table 1). The initial grains already presented  
320 some features of previous dissolution, but the surface of the grains was relatively smooth.  
321 After a few weeks, micro-stylolites developed at the contact between quartz grains, forming  
322 rough surfaces, while free faces only showed dissolution patterns (figure 10). These  
323 observations indicate that IPS was efficient under isostatic compaction even with very small  
324 amounts of water. However, the unknown and variable initial shape of the quartz grains  
325 precluded any quantification of the strain of individual grains, as done for the glass spheres.

326

## 327 **4 Discussion**

328 The aim of this study was to quantify the strain of the particles of an aggregate using a  
329 simple experimental design (isostatic confining pressure, constant temperature), for various P-  
330 T-t conditions and amounts of fluid. Deformation processes and the heterogeneity of the local  
331 stresses are discussed first. The experimental results are then compared with glass creep  
332 according to an exponential law and with the creep of natural minerals according to a power  
333 law. Finally, the implications of this experimental study are discussed for several geological  
334 fields where fluid-enhanced deformation under high P-T is relevant.

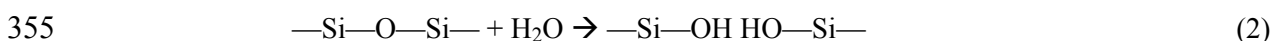
335

### 336 *4.1 Deformation processes*

337 Experiments were performed under P-T conditions suitable for IPS deformation in  
338 natural silica-rich rocks, but the experimental results obtained indicate that at least three main  
339 deformation processes occurred in the simple system used, involving only glass spheres +  
340 3 wt.% mica and pore water:

341 - *Brittle deformation* (cracking) occurred in all experiments, but the level of  
342 deformation depends primarily on the confining pressure and to a lesser extent on  
343 temperature.

344 - *Ductile deformation* was also observed in all experiments, illustrated in the dry  
345 experiments by the development of flat contacts due to plastic flow. This deformation process  
346 is very rapid and occurred at the very beginning of all experiments. Figure 7 shows that  
347 plastic flow was thermally activated, which is consistent with a decrease in effective glass  
348 viscosity with increasing temperature (figure 1). Plastic flow also occurred in the experiments  
349 conducted with water, as suggested by the flat outer rings bordering the contacts between the  
350 spheres in these experiments. Although glass hydration was not evidenced by Raman  
351 spectroscopy in the 1vol.% fluid experiments, the increase in strain with the addition of water  
352 is likely due to the decrease in effective glass viscosity resulting from partial hydration of the  
353 glass. Water affects glass by decreasing the connectivity of the network according to the  
354 following chemical reaction:



356 This reaction leads to the replacement of covalent chemical bonds by hydrogen bonds,  
357 thereby inducing a reduction in the effective glass viscosity. The observed enhancement of  
358 recrystallization with 1 vol.% fluid at  $T > 350^\circ\text{C}$  suggests that the hydration reaction of glass  
359 was thermally activated. However, another deformation process occurred in the experiments

360 with water. Given the shape of the inside surface of the contacts and the fact that spheres were  
361 often bonded together it would seem that not all the water entered the glass spheres, and that  
362 fluid-driven deformation, such as IPS, might also have been active in the 1 vol.% water  
363 experiments. Fluid-driven deformation was clearly less efficient than plastic flow at the  
364 beginning of the experiments. However, it became the dominant deformation mechanism in  
365 experiments lasting more than two weeks, once the contact between the spheres reached a  
366 critical size above which the local stress was too low for plastic deformation. In any case, the  
367 low amount of fluid was not a limiting factor for IPS, since it proved to be effective in the  
368 quartz bearing experiments with 1 vol.% water. The observations made in these experiments  
369 also suggest that, in the presence of a small amount of water, there is a critical contact size  
370 above which sintering occurred. This effect strengthened the aggregate and acted against  
371 further ductile deformation.

372 - *Chemical solid-fluid reactions* occurred at 450°C even for low fluid content and at  
373 350°C in the 5 vol.% fluid experiments. Under these conditions, the glass spheres crystallized  
374 and also dissolved on their free faces. This is reflected by the occurrence of reaction rims on  
375 free faces and by the presence of a new phase in the porosity (figures 3E-G). Assuming that  
376 the initial porosity of the aggregates was about 32% (based on a body-centered cubic  
377 packing), 5 vol.% and 1 vol.% of water filled respectively 14% and 3% of the porosity. The  
378 extent of the reaction was surprisingly high in view of the low amount of fluid involved in the  
379 experiments and considering that the transport of elements from the spheres toward the  
380 porosity has to take place by diffusion in a thin fluid layer confined at the grain contacts.  
381 Solid-fluid chemical reactions evidenced at 350°C in 5 vol.% experiments and at 450°C in  
382 1 vol.% experiments thus indicate that dissolution and precipitation kinetics, as well as  
383 transport kinetics in the fluid layer, were very high. The difference in experimental conditions  
384 between experiments showing almost no precipitation in the porosity (1 vol.% fluid at 350°C)  
385 and those showing a porosity almost completely filled with newly crystallized products  
386 (5 vol.% fluid at 350°C and 1 vol.% fluid at 450°C) indicates that the extent of fluid-glass  
387 interactions was closely dependent on both temperature and amount of fluid.

388

#### 389 4.2 *Heterogeneity of local stress in an aggregate*

390 Local normal stresses applied at the sphere contacts ( $\sigma_c$ ) at the end of the experiment  
391 were calculated from the size of the contact and the applied confining pressure using:

392 
$$\frac{\sigma_c}{d_s^2} = \frac{4\sigma}{\pi d_c^2} \quad (3)$$

393 where  $\sigma$  is the confining pressure (MPa),  $d_s$  the sphere diameter (m) and  $d_c$  the contact  
394 diameter (m). Local stresses were calculated for each contact and then averaged over the  
395 sample. According to the strain estimates given in table 1, porosity changes related to  
396 compaction were less than 2% of the initial porosity, so that changes in fluid pressure during  
397 compaction can reasonably be neglected. Furthermore, in experiments with 5 vol.% fluid with  
398 an initial 30% porosity, the pore pressure developed up to 350°C would be only up to a  
399 maximum of about 10 MPa, whereas at 450°C, under supercritical conditions it would be  
400 about 40 MPa. Consequently, the fluid pressure is much lower than the local stress at the  
401 grain contacts (table 1) and can therefore be neglected when estimating the effective stress at  
402 grain contacts according to equation 3.

403         Except for experiments performed at 400 MPa, cracking was only evidenced at a few  
404 contacts and was therefore observed to be a secondary deformation mechanism. Equation 3 is  
405 thus only suitable for calculating the local normal stress at plastically deformed contacts that  
406 were not fractured.

407         In all experiments, the dispersion of contact diameters is 2 to 7% of the average  
408 diameter (table 1), showing that the strain was heterogeneously distributed at grain scale in  
409 the samples. The calculated local stress dispersion is 5 to 30% of the averaged local stress,  
410 with most experiments having a lower heterogeneity with a dispersion of 5 to 15%. Even if  
411 these heterogeneities were observed at small scale, they average in the volume and the  
412 deformation at the sample scale was homogeneous. Consequently, using a sufficient number  
413 of microscopic measurements, a macroscopic constitutive flow law could be calculated for the  
414 aggregate.

415

#### 416 4.3 Comparison with creep of glass

417         The relative contributions of the three deformation mechanisms mentioned in part 4.1  
418 may have changed during the experiments, but they could have also been active at the same  
419 time. However, the results obtained indicate that strain was mostly accommodated by plastic  
420 flow, at least during the dry experiments and the first stage of the experiments with added  
421 water. Plastic deformation in glass cannot occur by the movement of dislocations as in  
422 crystallized material. Instead, deformation occurs by the rearrangement of groups of 10 to 100  
423 atoms. The macroscopic strain rate  $\dot{\epsilon}$  of plastic deformation in an amorphous material can be  
424 described by the following equation (Spaepen, 1981; Heggen *et al.*, 2004):

$$425 \quad \dot{\epsilon} = 2c_f k_f \frac{B}{\Omega} \sinh\left(\frac{B}{2kT} \sigma\right) \quad (4)$$

426 where  $\sigma$  is the external pressure,  $k_f$  is a rate constant,  $\Omega$  is the atomic volume,  $c_f$  is the  
 427 concentration of defects,  $k$  is the Boltzmann constant,  $T$  is the temperature, and  $B$  is the  
 428 activation volume. When  $\frac{B}{2kT}\sigma$  is high,  $\sinh\left(\frac{B}{2kT}\sigma\right)$  can be simplified to  $\frac{1}{2}\exp\left(\frac{B}{2kT}\sigma\right)$   
 429 and the strain equation 4 can be rewritten as a more classical exponential law.

$$430 \quad \dot{\epsilon} = AB \exp\left(\frac{B}{2kT}\sigma\right) \quad (5)$$

$$431 \quad \text{with } A = \frac{2c_f k_f}{\Omega}.$$

432 A plot of  $\dot{\epsilon}$  as a function of the local normal stress at the contact (figure 11) shows a  
 433 linear trend on a linear-log scale. Therefore, the experimental data can be reasonably  
 434 explained by an exponential law (equation 5). The slope of the  $\ln \dot{\epsilon} - \sigma$  lines in figure 11  
 435 corresponds to the values of  $B/2kT$ , which are respectively  $2.69 \pm 1.16 \times 10^{-9}$  and  $3.64 \pm 1.96$   
 436  $\times 10^{-9}$  for dry and wet experiments at 350°C. From these values, activation volumes  $B = 46 \pm$   
 437  $20 \text{ \AA}^3$  and  $B = 63 \pm 32 \text{ \AA}^3$  are obtained for the dry and wet experiments (table 2). In view of  
 438 the very wide scatter of the  $\ln \dot{\epsilon} - \sigma$  experimental data at 150°C, it was not possible to calculate  
 439 an activation volume from these data, so it was assumed that it was the same as at 350°C.

440 The pre-exponential factors derived from figure 11 for both the dry and wet  
 441 experiments at 350°C are:  $AB_{dry} = 1.91 \pm 1.32 \times 10^{-12} \text{ s}^{-1}$  and  $AB_{1vol\%} = 4.16 \pm 7.06 \times 10^{-13} \text{ s}^{-1}$ .  
 442 For the 150°C experiments, a value of  $AB = 5.69 \pm 41.03 \times 10^{-15} \text{ s}^{-1}$  was obtained for both the  
 443 dry and wet experiments, when using  $B = 46 \pm 29 \text{ \AA}^3$ . The increase in  $AB$  with temperature  
 444 corresponds to an increase in  $A$  from about  $10^{-16} \text{ \AA}^{-3} \cdot \text{s}^{-1}$  at 150°C to about  $10^{-14} - 10^{-15} \text{ \AA}^{-3} \cdot \text{s}^{-1}$  at  
 445 350°C in both the wet and dry experiments respectively. These variations quantify the joint  
 446 effect of temperature and water on the rate constant  $k_f$  in equation 4.

447 Figure 11 gives  $B_{1vol\%} > B_{dry}$  and  $A_{1vol\%} < A_{dry}$  (table 2). The presence of fluid in the  
 448 porosity and in the contact zone between two glass spheres is likely to affect the rate constant  
 449  $k_f$ , while  $c_f$  and  $\Omega$  remain constant. Therefore, figure 11 suggests that  $k_{f1vol\%} < k_{fdry}$ . However,  
 450 these experiments indicate that strain and strain rate are lower in dry experiments than in  
 451 experiments performed with 1vol.% fluid, suggesting that the rate constant  $k_f$  is larger in the  
 452 wet experiments. Assuming that the activation volume  $B$  is constant in both the dry and wet  
 453 experiments implies that  $A_{1vol\%} > A_{dry}$  and  $k_{f1vol\%} > k_{fdry}$ . Indeed, if as shown in figure 11, the  
 454 best fit of the  $\ln \dot{\epsilon} - \sigma$  data obtained at 350°C in the wet experiments is plotted using a fixed  $B =$   
 455  $46 \text{ \AA}^3$  (as obtained from the dry experiments),  $AB_{1vol\%} = 7.11 \pm 4.91 \times 10^{-12}$ , which

456 corresponds to  $A_{1vol\%} = 1.54 \pm 1.06 \times 10^{-13} \text{ \AA}^{-3} \cdot \text{s}^{-1}$ . This value of  $A$  is now higher than that  
 457 obtained for the dry experiments ( $A_{dry} = 4.06 \times 10^{-14} \text{ \AA}^{-3} \cdot \text{s}^{-1}$ ), which is consistent with an  
 458 increase in the rate constant  $k_f$  resulting from glass hydration. It is therefore likely that the  
 459 activation volumes of dry and hydrated glass are similar.

460 An interesting result is that the effective glass viscosity estimated as  $\eta_{eff} = \sigma / \dot{\epsilon}$  lies in  
 461 the range  $10^{15} - 10^{18} \text{ Pa}\cdot\text{s}$ . These values are in agreement with the extrapolation of the  
 462 viscosity of soda-lime glass measured at high temperature to the temperature of the  
 463 experiments described here (figure 1). Furthermore, the effective glass viscosity is higher in  
 464 dry than in wet experiments and in the  $150^\circ\text{C}$  experiments than those at  $350^\circ\text{C}$  (table 1).

465

#### 466 4.4 Comparison with power-law creep

467 Deformation of crystalline material at moderate temperature involves dislocation  
 468 creep, which is well described by a power-law. As mentioned above, glass deformation does  
 469 not involve the movement of dislocation and may be described by exponential creep laws.  
 470 However, in view of the large variation in strain rate with varying contact stresses (more than  
 471 a factor 100 increase in  $\dot{\epsilon}$  is observed when  $\sigma$  is doubled, see figure 11) and experimental  
 472 data scatter, it is reasonable to describe these experiments using a power law relationship.  
 473 Such a constitutive law is widely used for rocks subjected to stress and strain rates  
 474 corresponding to those of the crust (Poirier, 1985):

$$475 \quad \dot{\epsilon} = A_1 \exp\left(-\frac{E}{RT}\right) \sigma^n \quad (6)$$

476 with  $A_1$  and  $n$  being the power law parameters ( $A_1$  in  $\text{Pa}^{-n}\text{s}^{-1}$ ),  $E$  the activation energy  
 477 ( $\text{kJ}\cdot\text{mol}^{-1}$ ),  $R$  the gas constant ( $\text{kJ}\cdot\text{mol}^{-1}\text{K}^{-1}$ ) and  $T$  the temperature (K). The Arrhenius term  
 478 accounts for the increase in strain rate with temperature (figure 7). The validity of the power  
 479 law for the conditions of the experiments described here is demonstrated in figure 12, which  
 480 shows that the  $\log(\dot{\epsilon})-\log(\sigma)$  data for the different sets of experiments can be reasonably  
 481 fitted by a straight line.

482 The stress exponent and pre-exponential factors in equation 6 can be obtained from the  
 483 slope and the intercept of these plots. Figure 12 shows that the dry and wet experiments can  
 484 be fitted with the same stress exponent,  $n = 10.5 \pm 2.2$  at  $350^\circ\text{C}$ . These values are much  
 485 higher than those generally obtained for crystalline material deformed by dislocation creep at  
 486 similar conditions,  $n = 2$  to  $4$  for quartzite (Kronenberg & Tullis, 1984 and references therein;  
 487 Poirier, 1985; Koch *et al.*, 1989) and  $n = 5-8$  for salt (Poirier, 1985). However, the high stress



488 exponent deduced from the experiments is in reasonable agreement with those reported by  
489 Kingery *et al.* (1976) for glass (from 4 to 20) or for plasticine at room temperature (up to  $n =$   
490 7.3; Zulauf & Zulauf, 2004). Kronenberg & Tullis (1984) evidenced a decrease of the stress  
491 exponent with fluid availability, whereas this study show that both dry and wet experiments  
492 have similar stress exponent with similar uncertainties. However, one should note that the  
493 pre-factor  $A_1 \exp(-E/RT)$  of the power-law creep increases 5 times with the addition of water,  
494 from  $1.50 \pm 1.04 \times 10^{-108} \text{ Pa}^{-10.5} \text{ s}^{-1}$  in dry experiments to  $8.01 \pm 5.54 \times 10^{-108} \text{ Pa}^{-10.5} \text{ s}^{-1}$  in wet  
495 experiments. This evolution shows the strong enhancing effect of water on deformation rate.

496 The activation energy can be calculated using the intercepts ( $A_1 \exp(-E/RT)$  in  
497 equation 6) of the  $\log(\dot{\epsilon}) = f(\log(\sigma))$  fits obtained for the 150°C and 350°C experiments with  
498 the same stress exponent. Since the same  $\epsilon = f(t)_{[P,T]}$  function was used to fit the dry and wet  
499 experiments at 150°C (dashed line in figure 12), different activation energies are obtained  
500 when using the dry or wet experiments at 350°C. Values of  $E = 78 \text{ kJ.mol}^{-1}$  and  $96 \text{ kJ.mol}^{-1}$   
501 were obtained when using the dry and wet experiments respectively, assuming  $A_1$  is  
502 independent of temperature.  $A_1$  calculated values are thus  $4.82 \pm 42.16 \times 10^{-102} \text{ Pa}^{-10.5} \text{ s}^{-1}$  for  
503 dry glass and  $8.88 \pm 77.73 \times 10^{-100} \text{ Pa}^{-10.5} \text{ s}^{-1}$  for hydrated glass. For plastic processes such as  
504 dislocation creep, the availability of water accounts for a decrease in activation energy from  
505  $300 \text{ kJ.mol}^{-1}$  in vacuum-dried quartzite to 220-170  $\text{kJ.mol}^{-1}$  in “as is” samples down to 120-  
506  $150 \text{ kJ.mol}^{-1}$  in wet quartzites, and for a variable increase in the pre-exponential parameter  $A_1$   
507 (Kronenberg & Tullis, 1984 and references therein). The increase in the pre-exponential  
508 parameter  $A_1$  observed in this study is thus consistent with observations of dislocation creep  
509 of quartzite (Kronenberg & Tullis, 1984 and references therein; Koch *et al.*, 1989). Activation  
510 energies estimated here for plastic deformation of amorphous materials are 1.5-2 times lower  
511 than those estimated for crystalline materials, but they are similar to those of intergranular  
512 pressure-solution ( $73 \text{ kJ.mol}^{-1}$  Dewers & Hajash, 1995). The increase of the activation energy  
513 from wet to dry experiments is opposite to the variations reported in the literature for  
514 crystalline material. However, in view of the large uncertainties on the estimated activation  
515 energies, this apparent variation is not significant.

516

#### 517 4.5 Comparison with natural materials

518 Experiments with glass spheres indicate a complex deformation process involving  
519 mostly plastic flow. Plastic deformation of silica minerals occurs at high pressure and  
520 temperature, and can be enhanced in the presence of fluid due to chemical reactions. The

521 simple low-T experiments on glass spheres described here can thus be considered as a first  
522 order analogue for the macroscopic study of silicate deformation at higher P-T conditions.

523         Rock softening due to the presence of fluid is mostly evidenced in the continental crust  
524 in ductile shear zones where fluid circulation coupled with high-grade deformation changes  
525 the rock rheology (Boullier & Guéguen, 1975; Behrmann & Mainprice, 1987; Martelat *et al.*,  
526 1999; Zulauf *et al.*, 2002; Rosenberg & Stünitz, 2003). These experiments thus have  
527 implications in several geological fields where deformation is coupled with fluid-rock  
528 interaction under high P-T conditions.

529         This study shows that despite the competition of several deformation mechanisms,  
530 stresses are mostly accommodated by plastic deformation mechanisms in the first-stage of  
531 compaction. However, due to the increase in contact surface area with time, the local stresses  
532 and resulting plastic deformation efficiency decrease. In the long term, the local stresses are  
533 no longer high enough for plastic deformation to be efficient and, as a result, plastic-dominant  
534 deformation is replaced by IPS-dominant deformation. Similar coupling and long-term  
535 change from cataclastic flow in a short-time scale (seismic event) to plastic and IPS  
536 deformations at a longer time-scale (inter-seismic event) has been evidenced in fault gouges  
537 in association with faulting and fluid circulation (Gratier *et al.*, 2003; Boullier *et al.*, 2004).  
538 Similar experiments to those reported in this study could thus give insights into the  
539 interactions between fluid circulation and the mechanical behavior and evolution of fault  
540 gouge.

541         High-temperature deformation experiments indicate that creep is enhanced in the  
542 presence of partial melting (Dell'Angelo *et al.*, 1987; Scheuvens, 2002; Garlick & Gromet,  
543 2004). A mechanism change is observed under the same P-T conditions from dislocation  
544 creep to a process involving mass transfer by diffusion in the presence of a small amount of  
545 melt (< 20% melt, Dell'Angelo *et al.*, 1987; Rosenberg & Handy, 2000; Rosenberg, 2001).  
546 The strain rate is higher in the presence of melt because films of melt localized within the  
547 grain contact enhance the diffusion of dissolved material to the pores, a process equivalent to  
548 IPS. In these experiments, the presence of water in the porosity has the same effect as the  
549 presence of small amounts of melt in the porosity of HT rocks (< 20% melt). The use of glass  
550 spheres may thus allow analogous melt experiments to be performed using a simple  
551 experimental design as well as experiments at lower P-T conditions than usual melt  
552 experiments. The main advantage of this experimental set-up is that the initial aggregate  
553 geometry can be deconvoluted from the deformation state.

554 Another field of application for similar experiments such as those conducted here is  
555 the compaction of pyroclastic deposits. Deformation experiments of glass sphere aggregates  
556 at relevant P-T and water content conditions should provide the necessary data for modeling  
557 the deformation of pyroclastic material (Quane *et al.*, 2004; Quane & Russel, 2005; Roche *et*  
558 *al.*, 2005). Quane *et al.* (2004) conducted compaction experiments with glass beads under  
559 constant uniaxial strain rate as an analogue for the welding of pyroclastic material. As a  
560 complement to such experiments, the approach described here provides another framework  
561 for studying more realistic natural situations. The data from these experiments show that  
562 hydrated pyroclastic deposits would compact more than dry deposits because of the increase  
563 in plasticity due to glass hydration. Glass hydration and associated rheological changes thus  
564 increase the compaction rate and allow compaction at lower temperature than for dry  
565 materials. Furthermore, these experiments provide new constraints on the rheology of soda-  
566 lime glass, which is used for analogue modeling of volcanic processes (Quane *et al.*, 2004;  
567 Quane & Russell, 2005).

568

## 569 **5 Conclusion**

570 Isostatic compaction experiments were performed on quartz and glass sphere  
571 aggregates under mid-crustal P-T conditions (200 MPa and 350°C) in order to quantify grain-  
572 scale strain and to make a comparison with theoretical models of ductile deformation in  
573 granular analogues of rocks. The main advantage of this approach is that, using low-cost  
574 pressure vessels, more than sixty deformation experiments could be performed. This made it  
575 possible to test a wide range of confining pressures, temperatures, and amounts of fluid.

576 Under the experimental P-T conditions, quartz and glass spheres do not deform by the  
577 same process. Natural materials show evidence of intergranular pressure-solution (IPS), while  
578 experiments with glass spheres show evidence of both, brittle and ductile deformation  
579 processes. Even though experiments using glass spheres show little evidence of IPS, ductile  
580 strain by grain contact plastic flattening can be significant in systems subjected to isostatic  
581 pressure conditions. However, IPS is an efficient deformation mechanism in the quartz  
582 aggregates experiments in the presence of 1 to 3 vol.% water and in the absence of strong  
583 external deviatoric stress.

584 Dry experiments show that glass spheres accommodate stress concentrations by  
585 plastic strain. The addition of water in the porosity allows the local stresses to be  
586 accommodated by additional deformation mechanisms. The experiments described show that  
587 fluid-glass interactions can be very high, even with very low amounts of fluid at  $T > 250^{\circ}\text{C}$ .

588 Below this temperature, the influence of water on strain decreases rapidly, and no influence  
589 was found for long-duration experiments lasting up to two weeks at 150°C with a low fluid  
590 content. In contrast, a very high reactivity of glass with water was observed at 450°C, leading  
591 to the precipitation of new material filling all the porosity. The same observations were also  
592 made at 350°C, but in the presence of a larger (but still very low) amount of water. With a  
593 large amount of fluid, chemical processes are dominant due to very rapid kinetics of  
594 dissolution-transport-precipitation of the glass.

595 In dry and wet experiments, deformation of a glass sphere aggregate is accommodated  
596 mostly by plastic flow that can be described by either an exponential or a power law for the  
597 range of experimental conditions. With power-law creep, the presence of a small amount of  
598 water does not affect the stress exponent ( $n = 10.5$  in both the dry and 1 vol.% experiments at  
599 350°C), but leads to a decrease in the pre-factor.

600 This study clearly highlights the key effect of water, and to a lesser extent temperature,  
601 in rock softening. The simple experiments presented in this study can thus be used as a first  
602 approximation of natural silicate rocks deformed in the presence of fluid at high pressure and  
603 temperature, like for instance the deformation of partially molten-rocks, the compaction of  
604 pyroclastic deposits or the change in deformation mechanisms in a fault zone during the inter-  
605 seismic phase.

606

## 607 **Acknowledgements**

608 This work was supported by Dyethi-INSU, STREP-PCRD6 and PROCOPE programs.  
609 The authors are grateful to R. Schulz and H. Steigert for technical assistance in the  
610 hydrothermal laboratory, and to J. Herwig and H. Kemnitz for their technical assistance  
611 during SEM observations. Thanks are also due to J.P. Gratier and E. Lewin for interesting  
612 discussions, and to A. Niemeijer, E. Rutter, and an anonymous reviewer for their critical and  
613 constructive reviews.

614

## 615 **References**

- 616 Behrmann, J.H. and Mainprice, D., 1987. Deformation mechanisms in a high-temperature  
617 quartz-feldspar mylonite: evidence for superplastic flow in the lower crust. *Tectonophysics*  
618 **140**(2), 297-305.
- 619 Bos, B., Peach, C.J. and Spiers, C.J., 2000. Frictional-viscous flow of simulated fault gouge  
620 caused by the combined effects of phyllosilicates and pressure solution. *Tectonophysics*  
621 **327**(3-4), 173-194.

622 Bos, B. and Spiers, C.J., 2000. Effect of phyllosilicates on fluid-assisted healing of gouge-  
623 bearing faults. *Earth Planet. Sci. Lett.* **184**(1), 199-210.

624 Boullier, A.M. and Guéguen, Y., 1975. SP-mylonites: origin of some mylonites by  
625 superplastic flow. *Contrib. Mineral. Petrol.* **50**, 93-104.

626 Boullier, A.M., Fujimoto, K., Ito, H., Ohtani, T., Keulen, N., Fabbri, O., Amitrano, D.,  
627 Dubois, M. and Pezard, P., 2004. Structural evolution of the Nojima fault (Awaji Island,  
628 Japan) revisited from the GSJ drill hole at Hirabayashi. *Earth Planets Space* **56**, 1233-1240.

629 Burnham, C.W., Holloway, J.R. and Davis, F., 1969. The specific volume range of water in  
630 the range 1000 to 8900 bars, 20° to 900°C. *Am. J. Sci.* **267-A**, 70-95.

631 Dell'Angelo, L.N., Tullis, J. and Yund, R.A., 1987. Transition from dislocation creep to melt-  
632 enhanced diffusion creep in fine-grained granitic aggregates. *Tectonophysics* **139**, 325-332.

633 Dewers, T. and Ortoleva, P., 1995. Influences of clay minerals on sandstone cementation and  
634 pressure solution. *Geology* **19**, 1045-1048.

635 Dewers, T. and Hajash, A., 1995. Rate laws for water-assisted compaction and stress-induced  
636 water-rock interaction in sandstones. *J. Geophys. Res.* **100**(B7), 13093-13112.

637 Garlick, S.R. and Gromet, L.P., 2004. Diffusion creep and partial melting in high temperature  
638 mylonitic gneisses, hope Valley shear zone, New England Appalachians, USA. *J.*  
639 *metamorphic Geol.* **22**(1), 45-62.

640 Gratier, J.P. and Guiguet, R., 1986. Experimental pressure solution-deposition on quartz  
641 grains: the crucial effect of the nature of the fluid. *J. Struct. Geol.* **8**(8), 845-856.

642 Gratier, J.P., Renard, F. and Labaume, P., 1999. How pressure solution creep and rate  
643 fracturing processes interact in the upper crust to make it behave in both a brittle and  
644 viscous manner. *J. Struct. Geol.* **21**(8-9), 1189-1197.

645 Gratier, J.P., Favreau, P. and Renard, F., 2003. Modeling fluid transfer along California faults  
646 when integrating pressure solution crack sealing and compaction processes. *J. Geophys.*  
647 *Res.* **108** (B2), doi:10.1029/2001JB000380.

648 Gundersen, E., Dysthe, D.K., Renard, F., Bjørlykke, K. and Jamtveit, B., 2002. Numerical  
649 modelling of pressure solution in sandstone, rate-limiting processes and the effect of clays.  
650 In: de Meer, S., Drury, M.R., de Bresser, J.H.P. and Pennock, G.M., 2002. *Deformation*  
651 *Mechanisms, Rheology and Tectonics: Current status and future perspective*. Geological  
652 Society, London, Special Publications, 200, 41-60.

653 He, W., Hajash, A. and Sparks, D., 2003. Creep compaction of quartz aggregates: effects of  
654 pore fluid flow – a combined experimental and theoretical study. *Am. J. Sci.* **303**. 73-93.

655 Heggen, M., Spaepen, F. and Feuerbacher M., 2004. Plastic deformation of Pd<sub>41</sub>, Ni<sub>10</sub>Cu<sub>29</sub>P<sub>20</sub>

656 bulk metallic glass. *Mat. Sci. Engin.* **375-377**, 1186-1190.

657 Hickman, S.H. and Evans, B., 1995. Kinetics of pressure solution at halite-silica interfaces  
658 and intergranular clay films. *J. Geophys. Res.* **100** (B7), 13113-13132.

659 Keenan, J.H., Keyes, F.G., Hill, P.G. and Moore, J.G., 1969. *Steam Tables. Thermodynamic*  
660 *Properties of Water Including Vapor, liquid and Solid Phases.* John Wiley and Sons, Inc.  
661 156 p.

662 Kingery, W.D., Bowen, H.K. and Uhlman, D.R., 1976. *Introduction to ceramics, 2<sup>nd</sup> Edition.*  
663 John Willey & Sons, New York, 1032p.

664 Koch, P.S., Christie, J.M., Ord, A. and George R.D., Jr, 1989. Effect of water on rheology of  
665 experimentally deformed quartzite. *J. Geophys. Res.* **994**(B10), 13975-13996.

666 Kronenberg, A.K. and Tullis, J., 1984. Flow strengths of quartz aggregates: grain size and  
667 pressure effects due to hydrolytic weakening. *J. Geophys. Res.* **89**(B6), 4281-4297.

668 Lemée, C. and Guéguen, Y., 1996. Modelling of porosity loss during compaction and  
669 cementation of sandstones. *Geology* **24**, 875-878.

670 Martelat, J.E., Schulmann, K., Lardeaux, J.M., Nicollet, C. and Cardon, H., 1999. Granulite  
671 microfabrics and deformation mechanisms in southern Madagascar. *J. Struct. Geol.* **21**(6),  
672 671-687.

673 Niemeijer, A.R. and Spiers, C.J., 2002. Compaction creep of quartz-muscovite mixtures at  
674 500°C: preliminary results on the influence of muscovite on pressure-solution. In: de Meer,  
675 S., Drury, M.R., de Bresser, J.H.P. and Pennock, G.M., 2002. *Deformation Mechanisms,*  
676 *Rheology and Tectonics: Current status and future perspective.* Geological Society,  
677 London, Special Publications, 200, 61-71.

678 Niemeijer, A.R., Spiers, C.J. and Bos B., 2002. Compaction creep of quartz sand at 400-  
679 600°C: experimental evidence for dissolution-controlled pressure solution. *Earth Planet.*  
680 *Sci. Lett.* **195**, 261-275.

681 Poirier, J.P., 1985. *Creep of crystals: high temperature processes in metals, ceramics and*  
682 *minerals.* Cambridge University Press, Cambridge, 260p.

683 Quane, S.L., Russell, J.K. and Kennedy, L.A., 2004. A low-load, high-temperature  
684 deformation apparatus for volcanological studies. *Am. Min.* **89**, 873-877.

685 Quane, S.L. and Russell, J.K., 2005. Welding: insights from high-temperature analogue  
686 experiments. *J. Volcanol. Geotherm. Res.* **142**, 67-87.

687 Raj, R. and Chyung, C.K., 1981. Solution-precipitation creep in glass ceramics. *Acta*  
688 *Metallurgica* **29**, 159-166.

689 Renard, F., Park, A., Ortoleva, P. and Gratier, J.P., 1999. An integrated model for transitional

690 pressure solution in sandstones. *Tectonophysics* **312**, 97-115.

691 Renard, F., Gratier, J.P. and Jamtveit, B. 2000. Kinetics of crack-sealing, intergranular  
692 pressure solution, and compaction around active faults. *J. Struct. Geol.* **22**(10), 1395-1407.

693 Renard, F., Dysthe, D., Feder, J., Bjørlykke, K. and Jamtveit, B., 2001. Enhanced pressure  
694 solution creep rates induced by clay particles: experimental evidence in salt aggregates.  
695 *Geophys. Res. Lett.* **28** (7), 1295-1298.

696 Renton, J.J., Heald, M.T. and Cecil, C.B., 1969. Experimental investigation of pressure  
697 solution of quartz. *J. Sediment. Petrol.* **39**(3), 1107-1117.

698 Roche, O., Gilbertson, M.A., Phillips, J.C. and Sparks, R.S.J., 2005. Inviscid behaviour of  
699 fines-rich pyroclastic flows inferred from experiments on gas-particle mixtures. *Earth*  
700 *Planet. Sci. Lett.* **240**(2), 401-414.

701 Rosenberg, C.L., 2001. Deformation of partially molten granite: a review and comparison of  
702 experimental and natural case studies. *Int. J. Earth Sciences* **90**(1), 60-76.

703 Rosenberg, C.L. and Handy, M.K., 2000. Syntectonic melt pathways during simple shearing  
704 of a partially molten rock analogue (norcamphor-Benzamide). *J. Geophys. Res.* **105**(B2),  
705 3135-3149.

706 Rosenberg, C.L. and Stünitz, H., 2003. Deformation and recrystallisation of plagioclase along  
707 a temperature gradient: an example from the Bergell tonalite. *J. Struct. Geol.* **25**, 389-408.

708 Rutter, E.H., 1976. The kinetics of rock deformation by pressure-solution. *Phil. Trans. R. Soc.*  
709 *Lond.* **283**, 203-219.

710 Rutter, E.H., 1983. Pressure solution in nature, theory and experiment. *J. Geol. Soc. London*  
711 **140**, 725-740.

712 Rutter, E.H. and Wanten, P.H., 2000. Experimental study of the compaction of phyllosilicate-  
713 bearing sand at elevated temperature and with controlled pore water pressure. *J. Sedim.*  
714 *Res.* **70**(1), 107-116.

715 Rutter, E.H. and Brodie, K.H., 2004. Experimental grain-size sensitive flow of hot-pressed  
716 Brazilian quartz aggregates. *J. Struct. Geol.* **26**, 2011-2023.

717 Rybacki, E. and Dresen, G., 2000. Dislocation and diffusion creep of synthetic anorthite  
718 aggregates. *J. Geophys. Res.* **105**(B11), 26017-26036.

719 Scheuven, D., 2002. Metamorphism and microstructures along a high-temperature  
720 metamorphic field gradient: the north-eastern boundary of the Královský hvozd unit  
721 (Bohemian Massif, Czech Republic). *J. metamorphic Geol.* **20**, 413-428.

722 Spaepen, F., 1981. Defects in amorphous materials. Les Houches Lectures XXXV on Physics  
723 of Defects, North Holland Press, Amsterdam, 133-174.

724 Stünitz, H. and Tullis, J., 2001. Weakening and strain localization produced by syn-  
725 deformational reaction of plagioclase. *Int. J. Earth Sciences* **90**(1), 136-148.

726 Tada, R. and Siever, R., 1986. Experimental knife-edge pressure solution of halite. *Geochim.*  
727 *Cosmochim. Acta* **50**(1), 29-36.

728 Tada, R., Maliva, R. and Siever, R., 1987. A new mechanism for pressure solution in porous  
729 quartzose sandstone. *Geochim. Cosmochim. Acta* **51**, 2295-2301.

730 Tada, R and Siever, R., 1989. Pressure solution during diagenesis. *Ann. Rev. Earth Planet. Sci.*  
731 **17**, 89-118.

732 Tuttle, O.F., 1969. Two pressure vessels for silicate-water studies. *Geol. Soc. Am. Bull.* **60**,  
733 1727-1729.

734 Vidal, O., 1997. Experimental study of the stability of pyrophyllite, paragonite and sodic  
735 clays in a thermal gradient. *Eur.J. Mineral.* **9**, 123-140.

736 Vidal, O. and Durin, L., 1999. Aluminium mass transfer and diffusion in water at 400-550°C,  
737 2 kbar in the K<sub>2</sub>O-Al<sub>2</sub>O<sub>3</sub>-SiO<sub>2</sub>-H<sub>2</sub>O system driven by a thermal gradient or by a variation of  
738 temperature with time. *Minerl. Mag.* **63**(5), 633-647.

739 Wang, A., Jolliff, B.L. and Haskin L.A., 1999. Raman spectroscopic characterization of a  
740 highly weathered basalt: igneous mineralogy, alteration products, and a microorganism, *J.*  
741 *Geophys. Res.* **104**, 27067 -27077.

742 Weyl, P.K., 1959. Pressure solution and the force of crystallization. A phenomenological  
743 theory. *J. Geophys. Res.* **69**, 2001-2025.

744 Xiao, X., Wirth, R. and Dresen, G., 2002. Diffusion creep in anorthite-quartz aggregates. *J.*  
745 *Geophys. Res.* **107**(B11), 2279-2293.

746 Yasuhara, H., Elsworth, D. and Polak, A., 2003. A mechanistic model for compaction of  
747 granular aggregates moderated by pressure solution. *J. Geophys. Res.* **108**, 2530,  
748 doi:10.1029/2003JB002536.

749 Zulauf, G., Dörr, W., Fiala, J., Koktová, J., Maluski, H. and Valverde-Vaquero, P., 2002.  
750 Evidence for high-temperature diffusional creep preserved by rapid cooling of lower crust  
751 (North Bohemian shear zone, Czech Republic). *Terra Nova* **14**, 343-354.

752 Zulauf, J. and Zulauf, G., 2004. Rheology of plasticine used as rock analogue: the impact of  
753 temperature, composition and strain.. *J. Struct. Geol.* **26**, 725-737.

754



755 **Figures**

756 Figure 1: Comparison of the viscosity of several kinds of glass versus temperature. Some  
757 characteristic temperatures are also reported:

758 - melting temperature ( $T_m$ ,  $\eta = 10$  Pa.s) below which glass is a liquid.

759 - working range ( $\eta = 10^3$ - $10^4$  Pa.s) for which glass is easily deformed.

760 - softening temperature ( $\eta = 4 \times 10^6$  Pa.s) which is the maximum temperature for which a  
761 glass sample does not flow under its own load.

762 - glass transition temperature ( $T_g$ ,  $\eta = 2 \times 10^{11}$  Pa.s) corresponds to the transition from  
763 supercooled liquid to solid glass.

764 - annealing temperature ( $\eta = 10^{12}$  Pa.s) at which glass releases its internal stress (by solid  
765 diffusion).

766 - strain temperature ( $\eta = 3 \times 10^{13}$  Pa.s) below which brittle deformation occurs before  
767 plastic deformation.

768 Under the experimental conditions of the present study ( $T < 450^\circ\text{C}$ ) the viscosity of soda-  
769 lime glass used (bold curve) is higher than  $10^{15}$  Pa.s, thus indicating that elastic brittle  
770 deformation occurred in addition to viscous flow (modified from a document from a  
771 lecture by L.V. Zhigilei at University of Virginia:  
772 <http://www.people.virginia.edu/~lz2n/mse209/Chapter14.pdf>).

773

774 Figure 2: Experimental set-up: A) Sample of glass spheres and fluid with controlled  
775 composition encapsulated within a 2mm internal diameter and 20 mm long gold capsule  
776 (thickness of the walls: 0.2 mm). The confining pressure medium was water. B) The cold  
777 pressure vessel is located within a horizontal heating system. The confining pressure is  
778 controlled with water.

779

780 Figure 3: SEM-pictures showing the contact morphology in a glass sphere aggregate in  
781 experiments performed at 200 MPa and  $350^\circ\text{C}$ . A. Flat contacts in dry experiments (Gm2).  
782 In experiments with 1 vol.% fluid, three types of contacts are observed: B. Contacts with  
783 bonding at the core and a flat rim (GmW3), C. Concentric rims of outgrowths and  
784 depressions (GmW12), and D. Stylolite-like contacts (GmW12). E. Filled porosity in  
785 5 vol.% fluid experiments; a similar structure is also observed at  $450^\circ\text{C}$  with 1 vol.% fluid  
786 (GmW4). F. Filled porosity in 5 vol.% fluid experiments. Microporous recrystallized  
787 material, interpreted as Ca-rich zeolites, completely fill the porosity (GmW9). G. Filled  
788 porosity in 14 vol.% fluid experiments (ENS2). Increasing the amount of water increases

789 the degree of reactivity and recrystallization of the spheres. With 15 vol.% fluid (G), the  
 790 spheres are entirely recrystallized, whereas with 5 vol.% fluid (E, F) recrystallization only  
 791 occurs at the rims and in 1 vol.% fluid experiments (B, C, D, H) no recrystallization is  
 792 evidenced. H. Initiation of fractures (arrows) that radiate from one contact to the others  
 793 (GmW16).

794

795 Figure 4: Raman spectra within the glass spheres of experiments performed at 200 MPa and  
 796 350°C. a) Spectra of the water content within the material. b) Spectra of the glass spheres  
 797 and recrystallized material. A. Overview of the difference between experiments: in black an  
 798 initial dry glass sphere (starting material), in grey a glass sphere from 1 vol.% fluid  
 799 experiment (GmW1), and in light grey recrystallized material from the porosity of 5 vol.%  
 800 fluid experiment (GmW4). B. Profiles over a distance of 32  $\mu\text{m}$  from within the glass  
 801 spheres (bottom) through the recrystallized material (top) in the porosity of an experiment  
 802 with 5 vol.% fluid (GmW4). The average spacing between successive measurement points  
 803 is about 4  $\mu\text{m}$ . On all the graphs, the different spectra have been shifted vertically for more  
 804 clarity.

805

806 Figure 5: Raman spectrum of a Ca-bearing Zeolite (thomsonite, from Wang *et al.* 1999).

807

808 Figure 6: A) Sketch to illustrate the method of calculating deformation at the grain contact  
 809 using the initial sphere diameter ( $d_s$ ) and the diameter of the truncated contact ( $d_c$ ). B.  
 810 Time-dependent change in the average 1-D strain for dry (empty symbols) and 1 vol.% fluid  
 811 (full symbols) experiments performed at 150°C and 350°C ( $P = 200$  MPa, circles and  
 812 squares respectively). The curves represent mean-square regression fits of the experimental  
 813 data following a power law.  $R$  is defined as the correlation coefficient using:

$$814 \quad R = \frac{\text{cov}(X, Y)}{\sigma_X \sigma_Y}, \text{ and } \text{cov}(X, Y) = \frac{1}{n} \sum_{j=1}^n (X_j - \bar{X})(Y_j - \bar{Y}) \text{ where } \bar{X} \text{ and } \bar{Y} \text{ are the average}$$

815 values of  $X$  and  $Y$  and  $\sigma_X$  and  $\sigma_Y$  are the standard deviations.

816

817 Figure 7: Change in the average contact deformation of dry (grey diamonds) and 1 vol.% fluid  
 818 (black diamonds) experiments versus temperature ( $P = 200$  MPa). The full lines represent  
 819 mean-square regression fits of the experimental data using an exponential law. Error bars  
 820 represent the standard-deviation normalized to the average strain.  $R$  is defined as in figure  
 821 6.

822

823 Figure 8: Change in the average contact deformation of dry (grey diamonds) and 1 vol.% fluid  
824 (black diamonds) experiments versus confining pressure ( $T = 350^{\circ}\text{C}$ ). The full lines  
825 represent fits mean-square regression of the experimental data using a linear law. Error bars  
826 represent the standard-deviation normalized to the average strain. R is defined as in figure  
827 6.

828

829 Figure 9: Evidence of dissolution and indentation at the contact between glass spheres and  
830 mica from SEM-pictures. A) Mica mechanical indentation in a dry experiment (Gm2). B)  
831 Kinked mica and broken spheres in a 1 vol.% experiment (GmW2). C) Dissolution of a  
832 glass sphere at the contact with a mica flake in experiment with 1 vol.% water (black arrow,  
833 GmW10). D) Dissolution of a glass sphere at the contact with a mica flake in an experiment  
834 with 5 vol.% water (white arrow, GmW11).

835

836 Figure 10: Dissolution patterns on quartz grains (QmW10). A) Morphology of a contact  
837 between two quartz grains showing evidence of intergranular pressure solution (micro-  
838 stylolite). The small debris are produced by grain crushing under brittle deformation. B)  
839 View of the quartz aggregate and the previous contact.

840

841 Figure 11: Strain rate ( $\text{s}^{-1}$ ) versus contact (local) stress (GPa) for both dry (empty symbols)  
842 and 1 vol.% experiments (full symbols) performed at  $150^{\circ}\text{C}$  and  $350^{\circ}\text{C}$  (circles and squares  
843 respectively) using an exponential deformation law ( $\ln \dot{\epsilon}$  versus  $\sigma$ , from equation 5). The  
844 black lines represent exponential fits of all experiments assuming a constant slope for  
845  $B = 56 \text{ \AA}^3$  (see text for more explanations). The full lines represent fits of 1 vol.% fluid  
846 experiments at  $350^{\circ}\text{C}$ , the dashed line the fit of dry experiments at 350, and the dotted line  
847 the fit of both dry and 1vol.% fluid experiments at 150. The grey line is the best  
848 exponential fit of the experiments performed with 1vol.% fluid ( $B = 69 \text{ \AA}^3$ ). The fits and  
849 regression equations are given in SI units ( $\sigma$  in Pa). R is defined as in figure 6.

850

851 Figure 12: Strain rate ( $\text{s}^{-1}$ ) versus stress (Pa) for both dry and 1 vol.% experiments performed  
852 at  $150^{\circ}\text{C}$  and  $350^{\circ}\text{C}$  following a power law ( $\ln \dot{\epsilon}$  versus  $\ln \sigma$ , from equation 6). The full  
853 and dashed lines represent the best exponential fits of 1 vol.% fluid experiments and dry  
854 experiments, respectively. These two lines have the same slope ( $n = 10.5$ ). Experiments  
855 performed at  $150^{\circ}\text{C}$  are fitted using  $n = 10.5$  as for the  $350^{\circ}\text{C}$  experiments. Dry and 1vol.%

856 experiments are fitted with the same power law. The fits and regression equations are given  
857 in SI units ( $\sigma$  in Pa). R is defined as in figure 6.

858

859 **Tables**

860 Table 1: Data of experiments performed with glass spheres and quartz grains.

861 Table 2: Deformation law parameters.

Figure 1  
[Click here to download high resolution image](#)

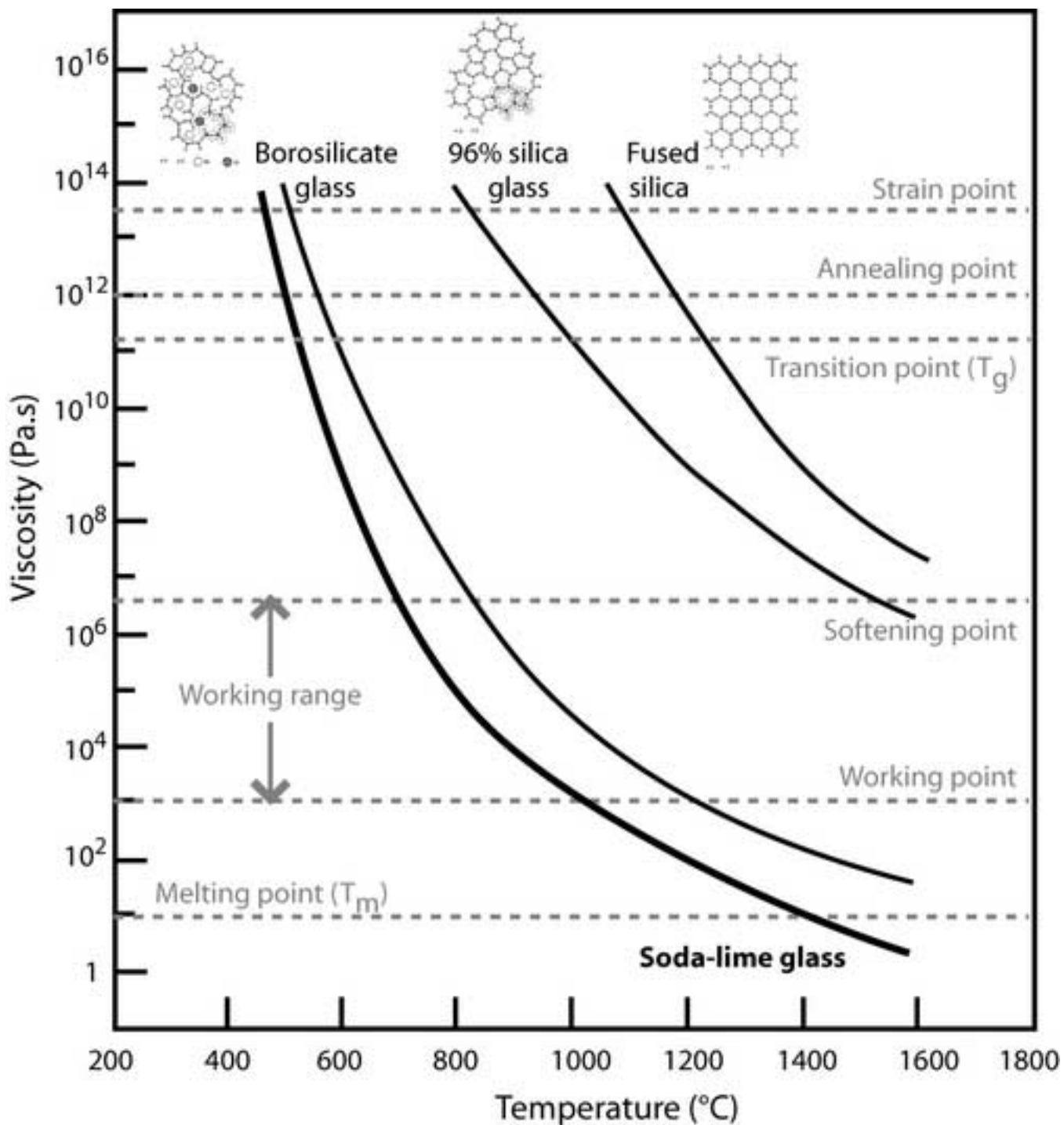


**Figure 2**  
[Click here to download high resolution image](#)

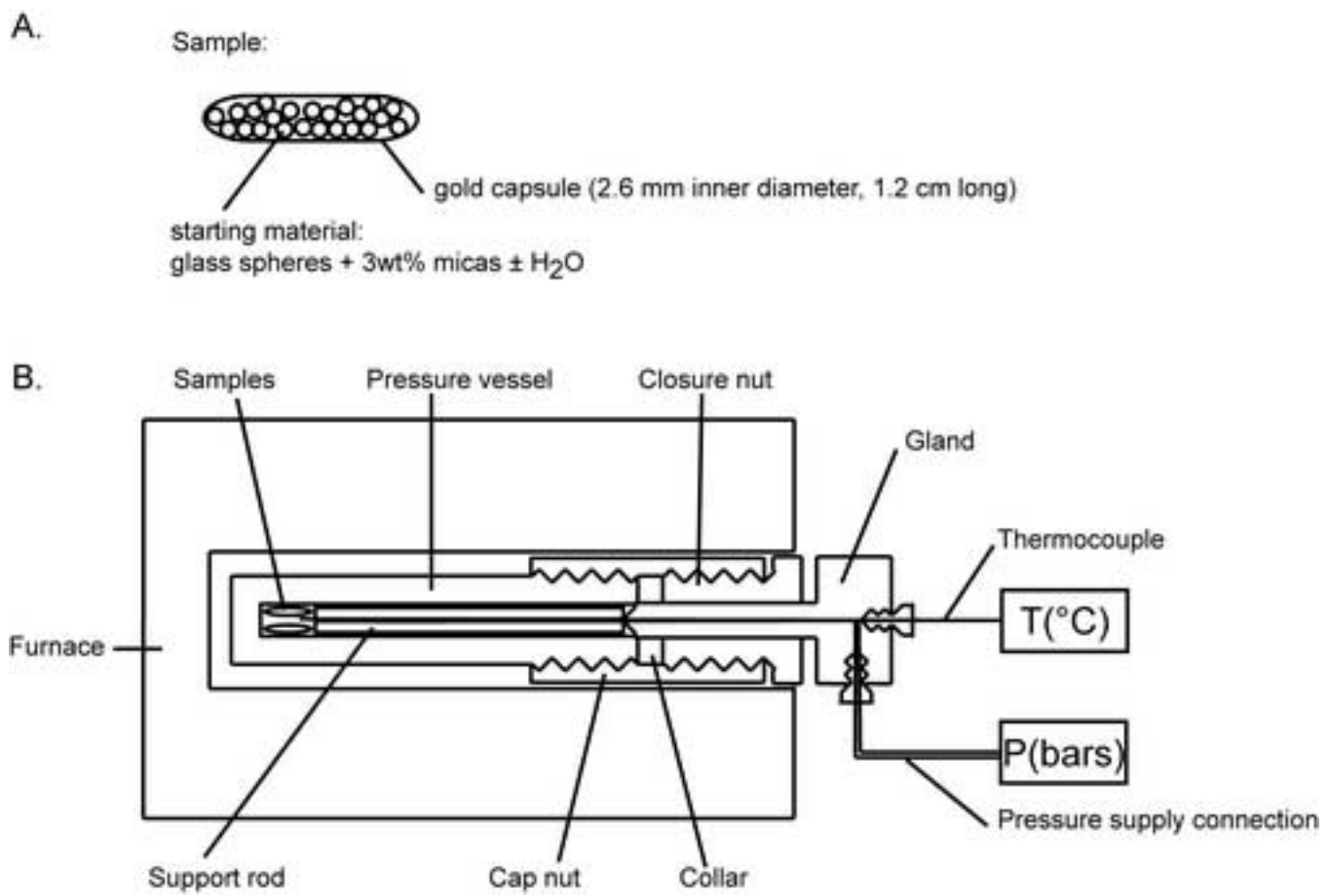


Figure 3  
[Click here to download high resolution image](#)

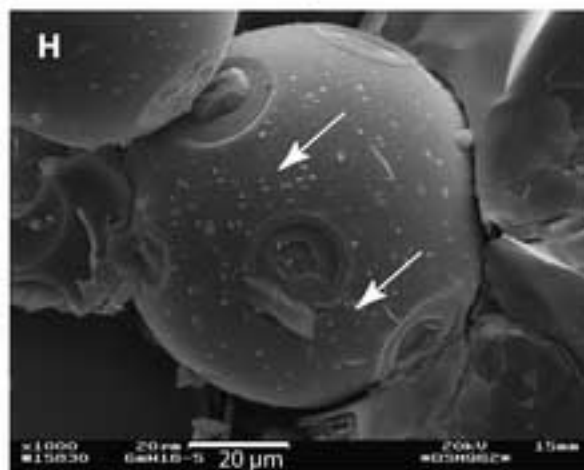
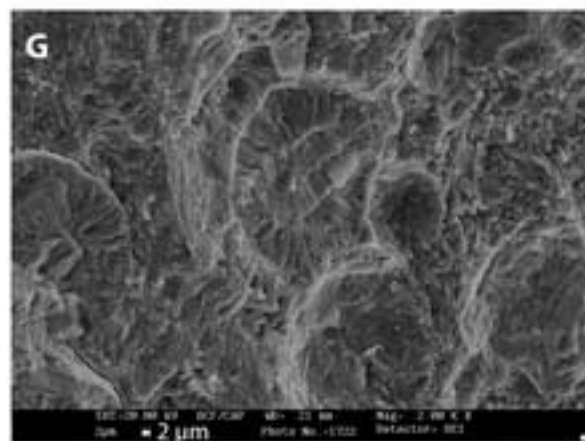
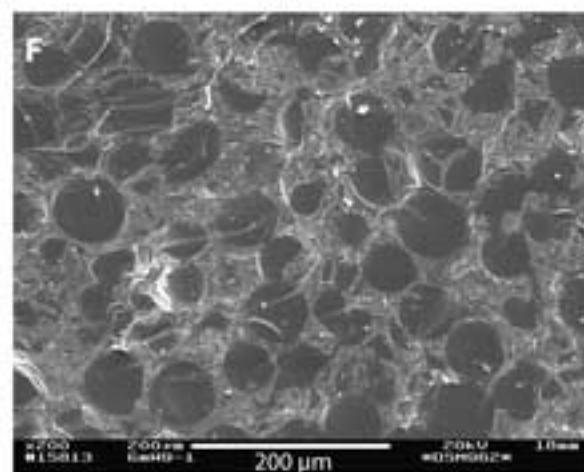
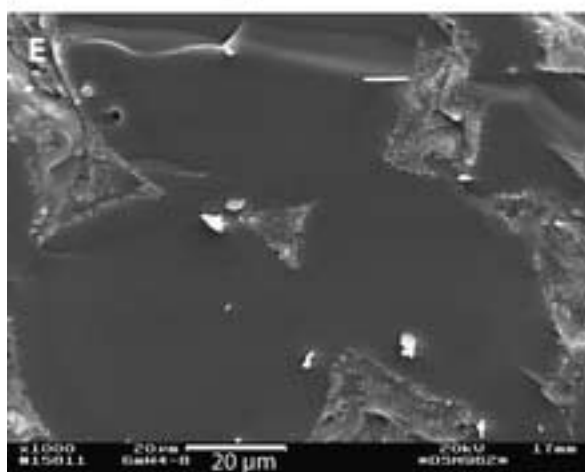
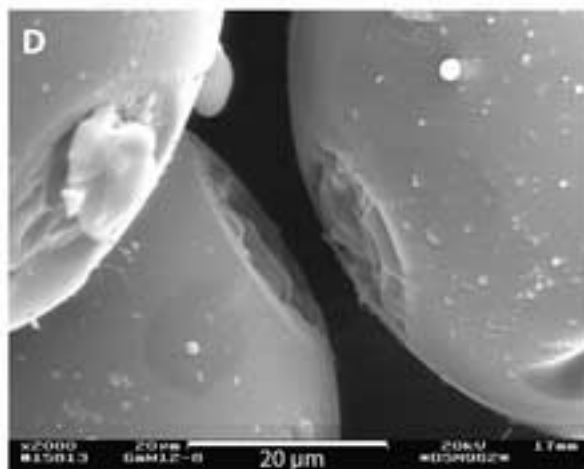
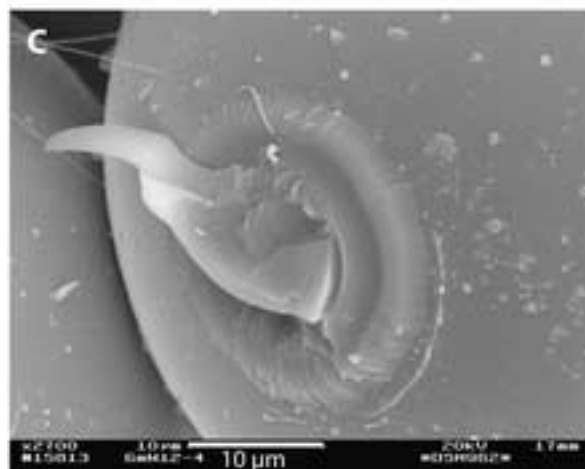
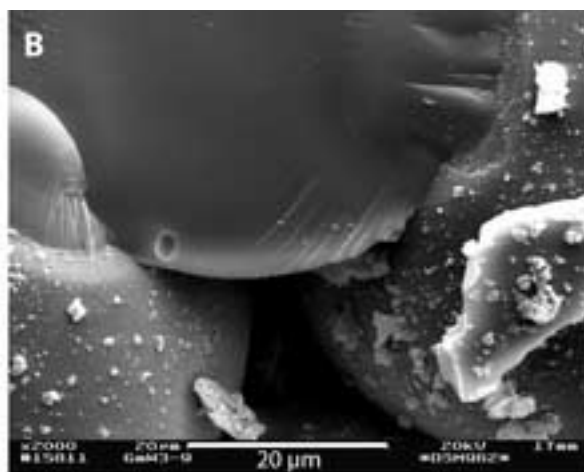
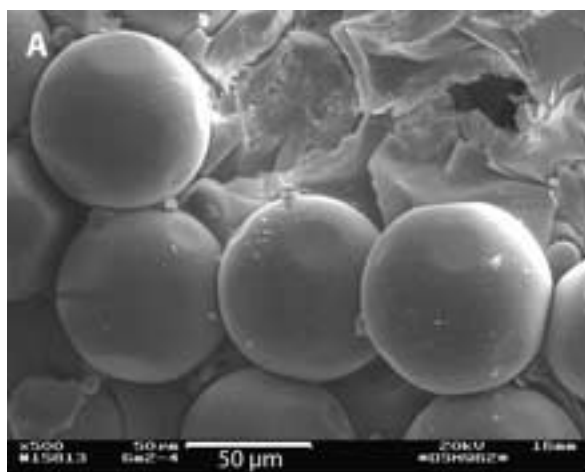


Figure 4

[Click here to download high resolution image](#)

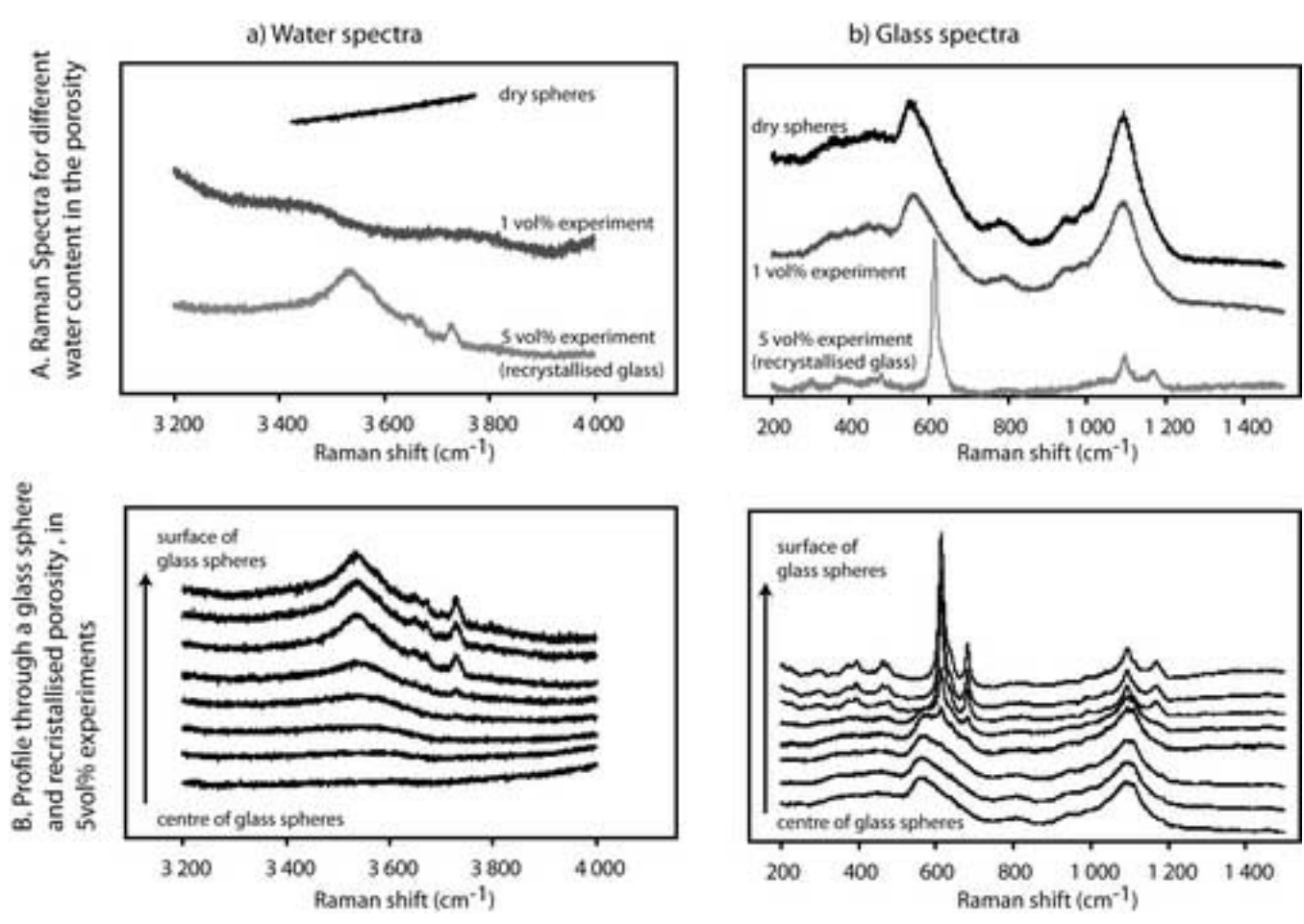




Figure 5  
[Click here to download high resolution image](#)

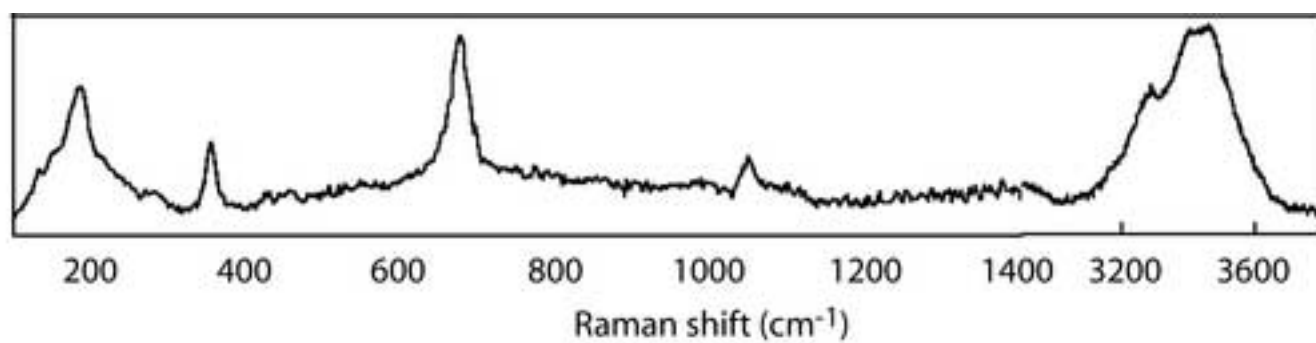


Figure 6  
[Click here to download high resolution image](#)

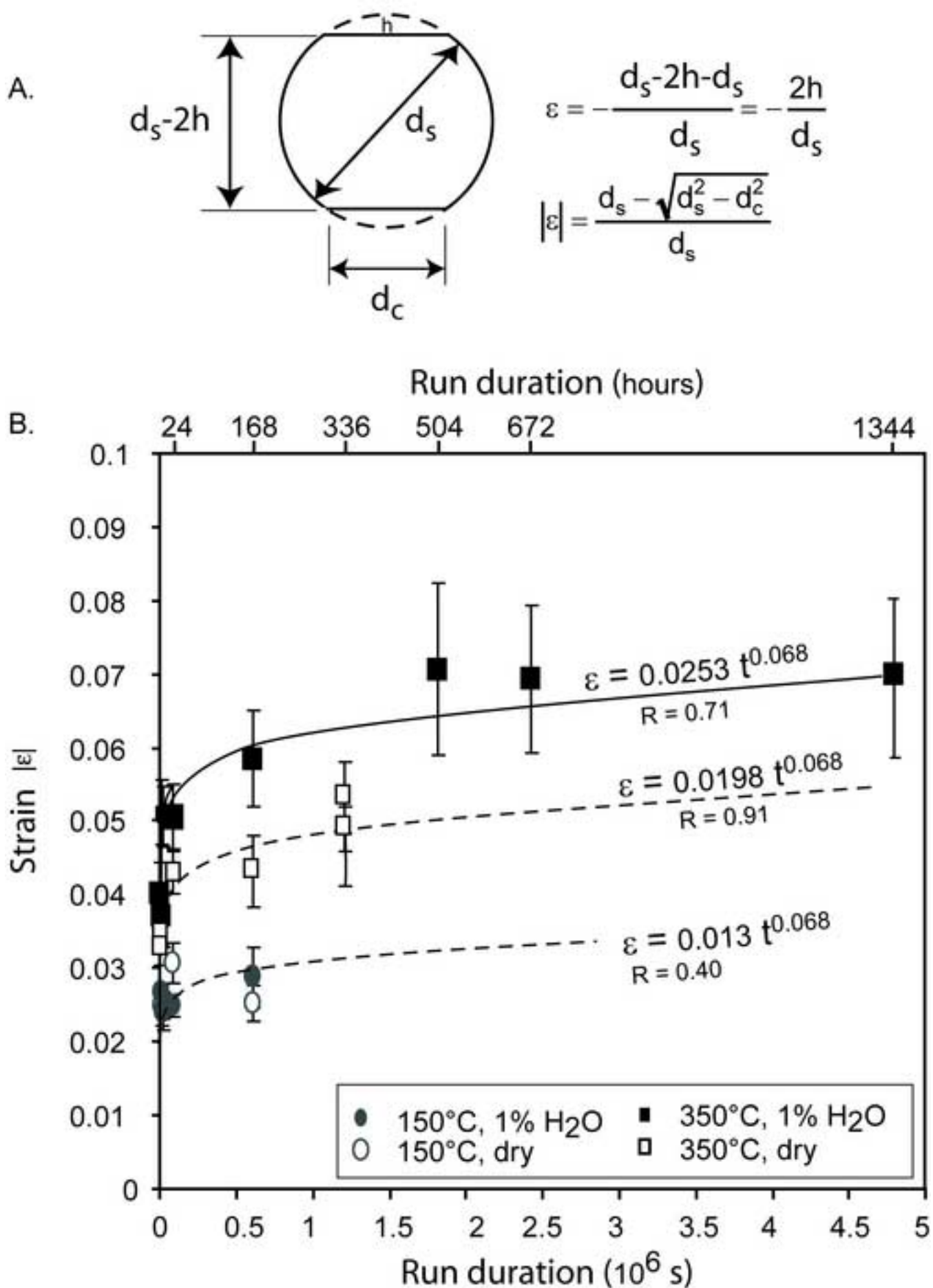


Figure 7  
[Click here to download high resolution image](#)

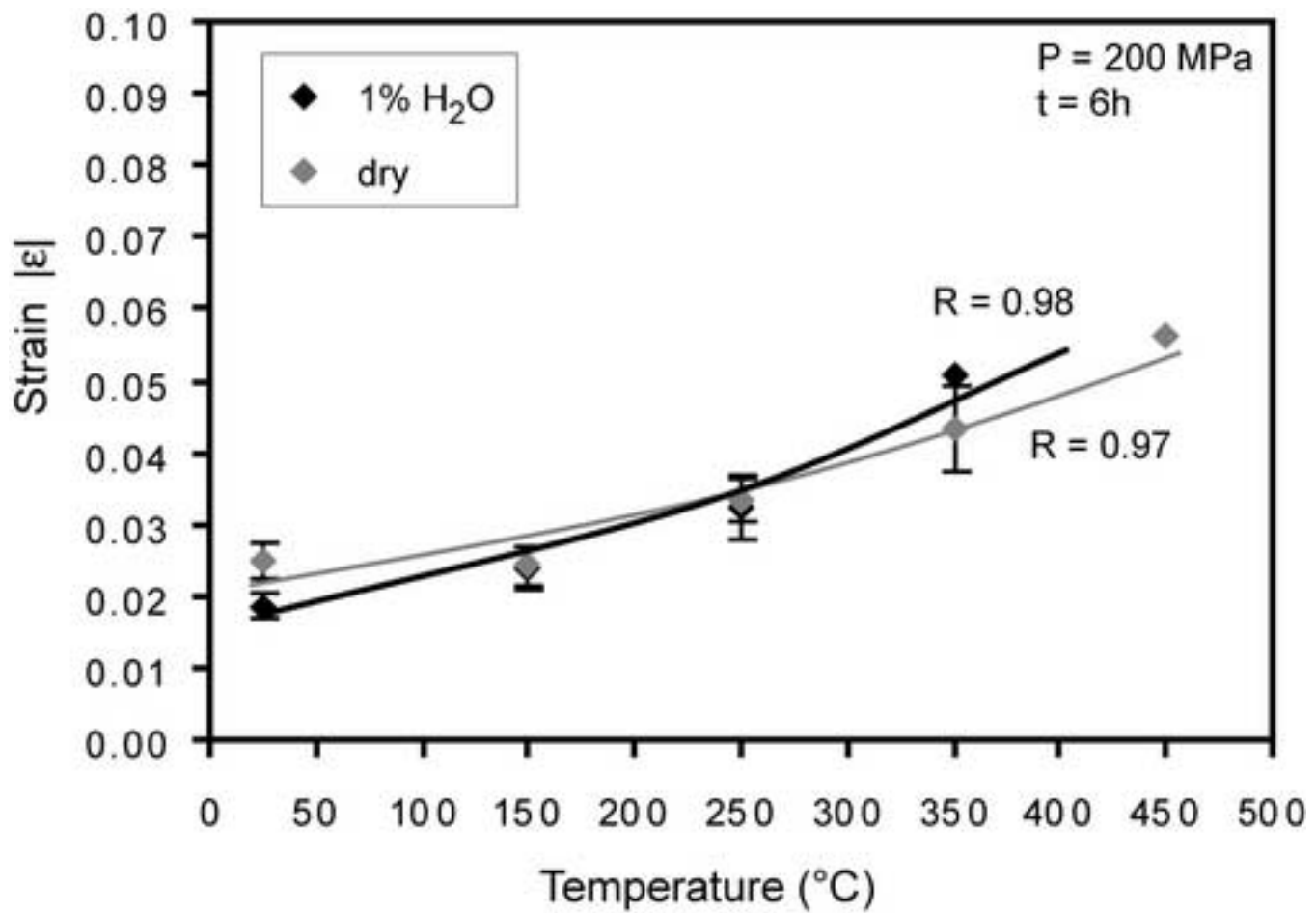


Figure 8  
[Click here to download high resolution image](#)

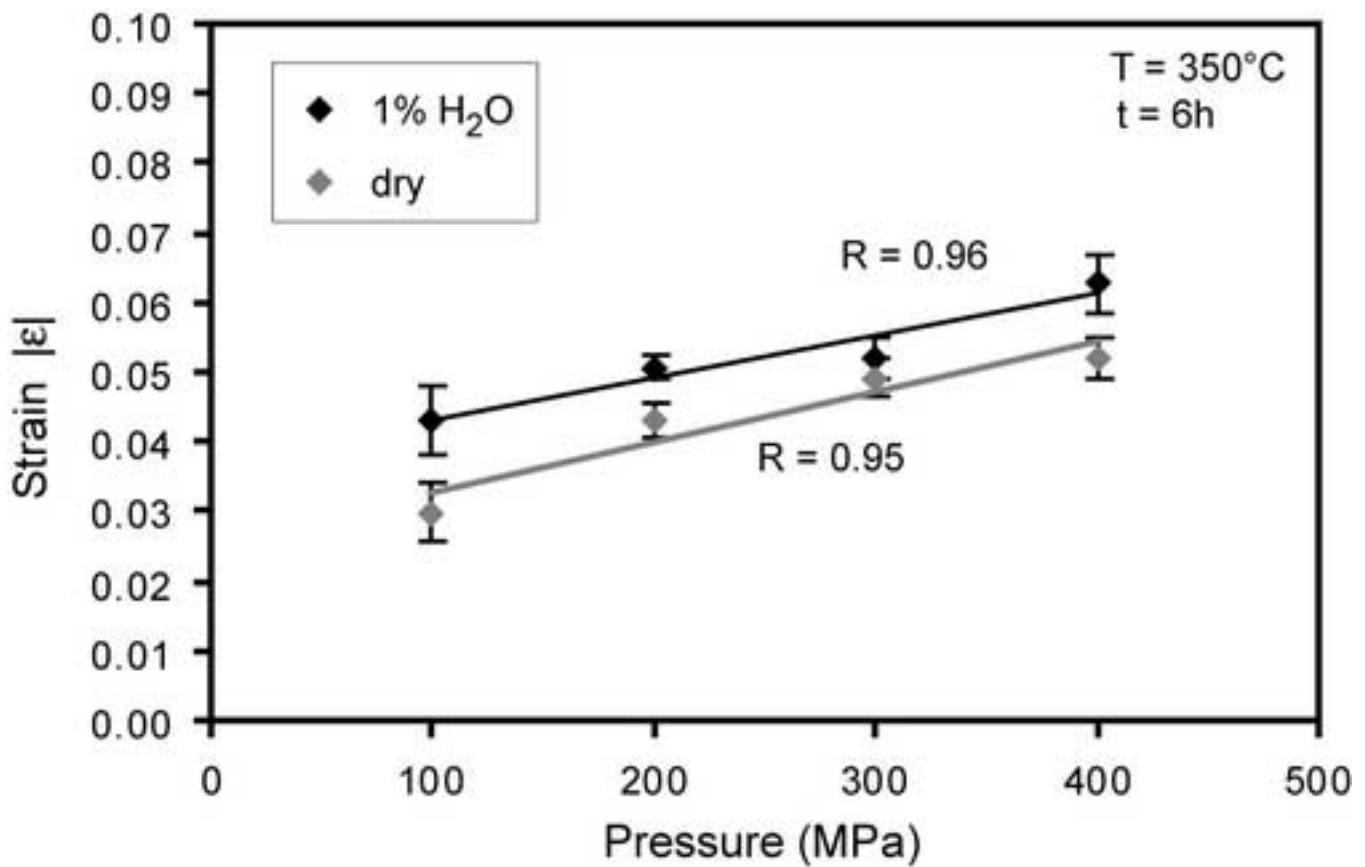


Figure 9  
[Click here to download high resolution image](#)

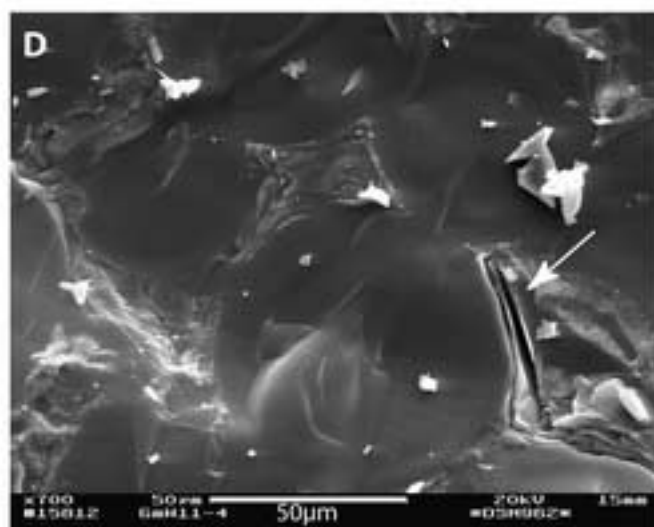
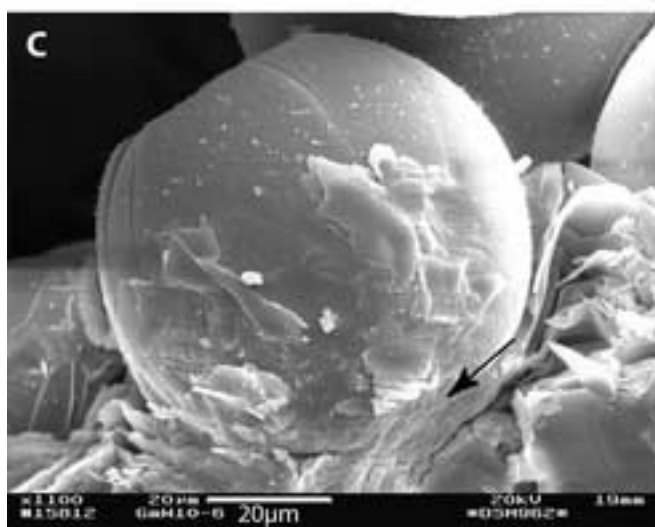
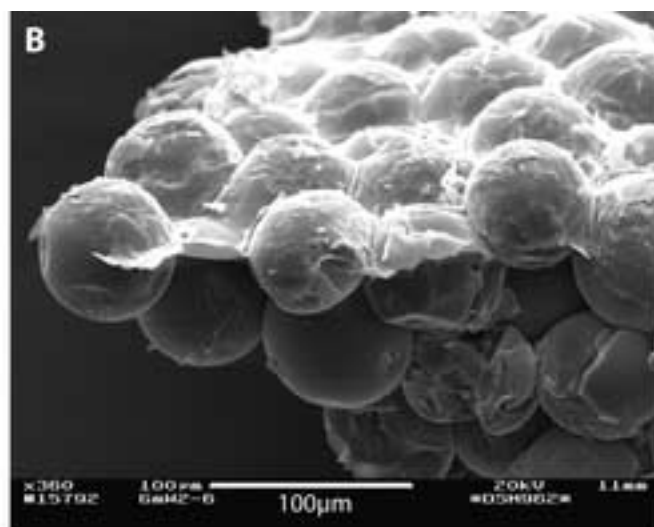
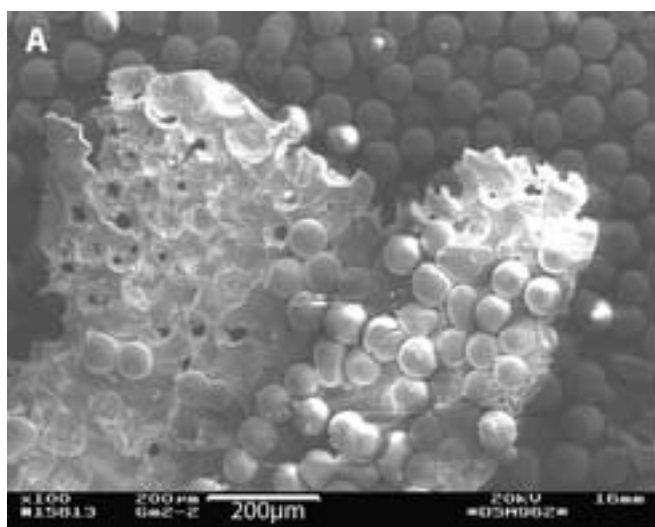


Figure 10

[Click here to download high resolution image](#)

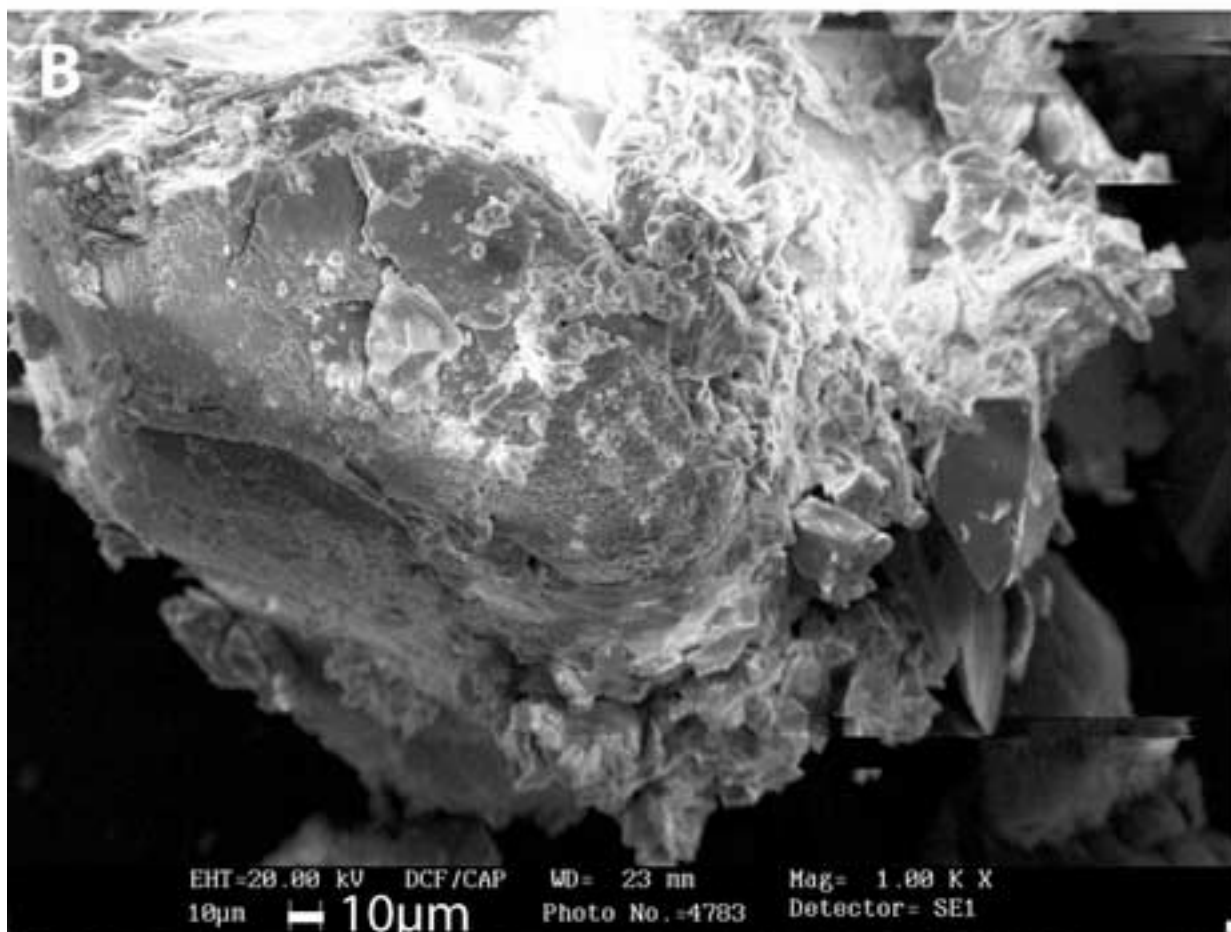
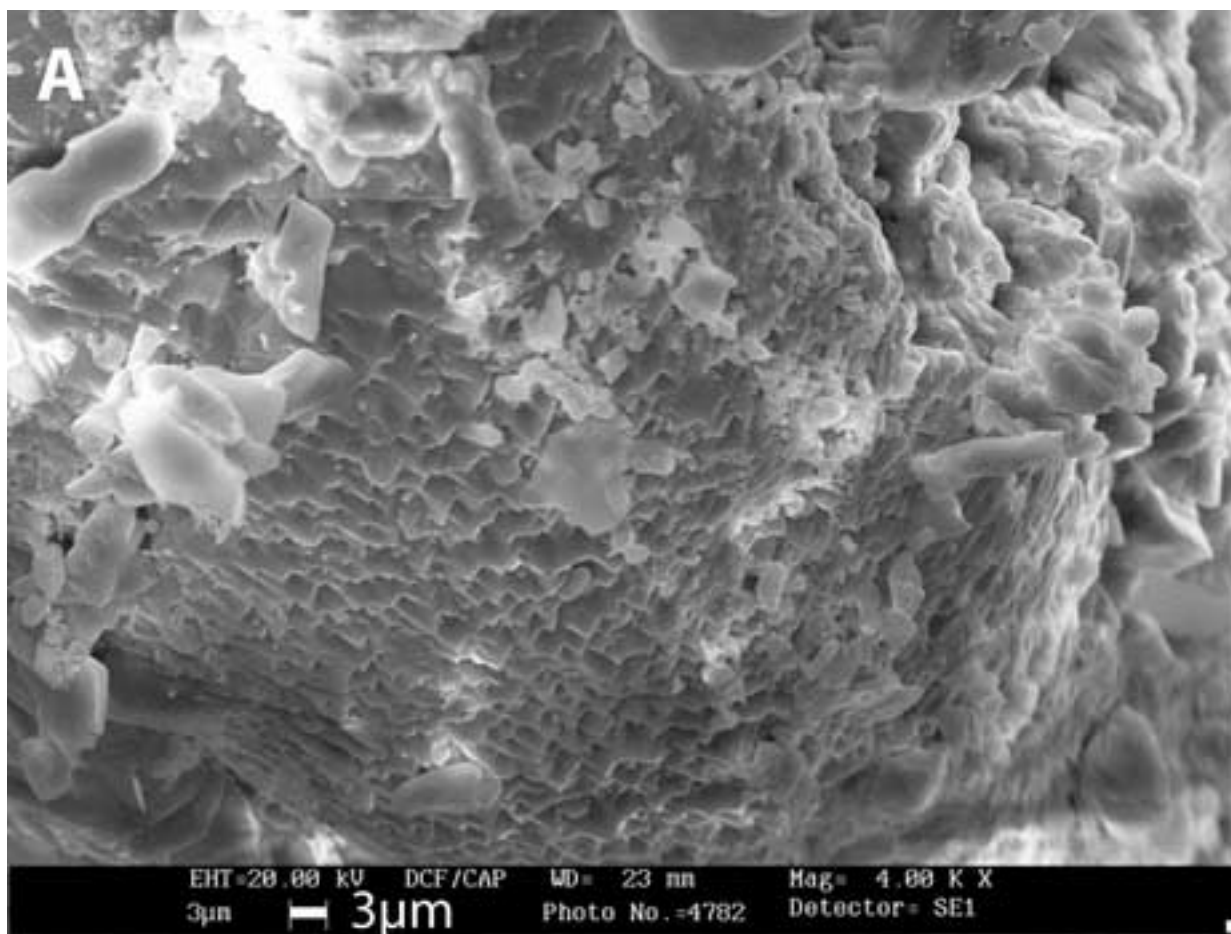


Figure 11

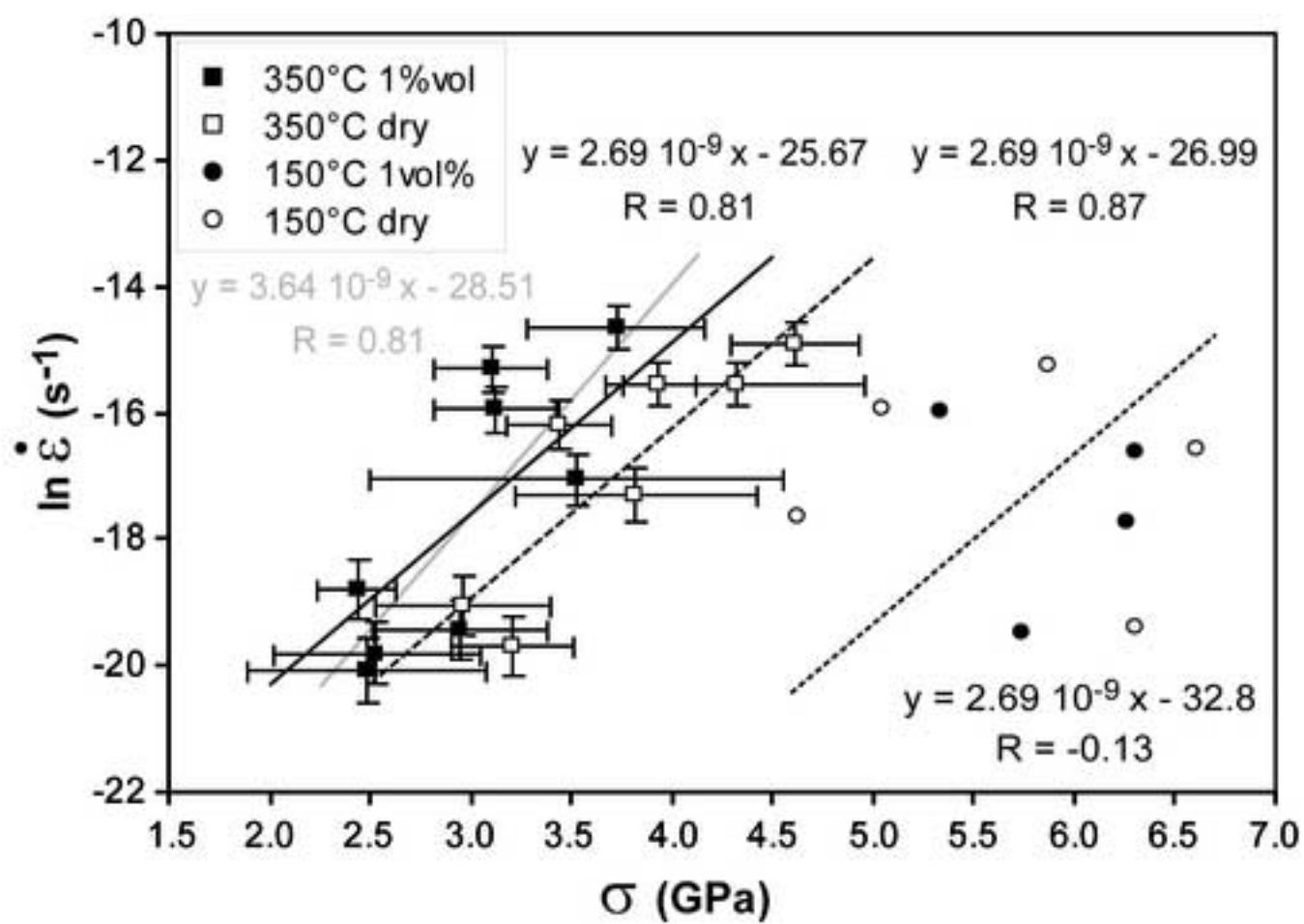
[Click here to download high resolution image](#)

Figure 12

[Click here to download high resolution image](#)

